



Open Archive Toulouse Archive Ouverte (OATAO)

OATAO is an open access repository that collects the work of some Toulouse researchers and makes it freely available over the web where possible.

This is an author's version published in: <https://oatao.univ-toulouse.fr/18497>

Official URL : <http://dx.doi.org/10.1007/s11214-017-0409-x>

To cite this version :

Mimoun, David and Murdoch, Naomi and Lognonné, Philippe and Hurst, Kenneth and Pike, William T. and Hurley, Jane and Nébut, Tanguy and Banerdt, William B. The Noise Model of the SEIS Seismometer of the InSight Mission to Mars. (2017) Space Science Reviews. pp. 1-46. ISSN 0038-6308

Any correspondence concerning this service should be sent to the repository administrator:

tech-oatao@listes-diff.inp-toulouse.fr

The Noise Model of the SEIS Seismometer of the InSight Mission to Mars

David Mimoun¹ · Naomi Murdoch¹ · Philippe Lognonné² · Kenneth Hurst³ · William T. Pike⁴ · Jane Hurley⁵ · Tanguy Nébut² · William B. Banerdt³ · SEIS Team⁶

Abstract The SEIS (Seismic Experiment for Interior Structures) instrument on board the InSight mission to Mars is the critical instrument for determining the interior structure of Mars, the current level of tectonic activity and the meteorite flux. Meeting the performance requirements of the SEIS instrument is vital to successfully achieve these mission objectives. The InSight noise model is a key tool for the InSight mission and SEIS instrument requirement setup. It will also be used for future operation planning. This paper presents

✉ D. Mimoun
david.mimoun@isae.fr

N. Murdoch
naomi.murdoch@isae.fr

P. Lognonné
lognonne@ipgp.fr

K. Hurst
Ken.Hurst@jpl.nasa.gov

W.T. Pike
w.t.pike@imperial.ac.uk

J. Hurley
hurley@atm.ox.ac.uk

T. Nébut
tanguy.nebut@ipgp.fr

W.B. Banerdt
william.b.banerdt@jpl.nasa.gov

- ¹ DEOS/SSPA, Institut Supérieur de l'Aéronautique et de l'Espace, Supaero, Université de Toulouse, 10, avenue Edouard Belin, 31055 Toulouse Cedex, France
- ² Institut de Physique du Globe de Paris, Sorbonne Paris Cité, Université Paris Diderot, 75013, Paris, France
- ³ Jet Propulsion Laboratory, California Institute of Technology, 4800 Oak Grove Drive, Pasadena, CA 91109, USA
- ⁴ Department of Electrical and Electronic Engineering, Imperial College London, South Kensington Campus, London SW7 2AZ, UK

the analyses made to build a model of the Martian seismic noise as measured by the SEIS seismometer, around the seismic bandwidth of the instrument (from 0.01 Hz to 1 Hz). It includes the instrument self-noise, but also the environment parameters that impact the measurements. We present the general approach for the model determination, the environment assumptions, and we analyze the major and minor contributors to the noise model.

Keywords InSight · SEIS · Noise model · Seismometer · Mars · Environment

Table 1 List of acronyms and terminology

Acronym	Meaning
APSS	Auxiliary Payload Sensor Suite
CNES	French Space Agency
DLR	German Space Agency
E-BOX	Electronics box for SEIS
EMC	Electromagnetic compatibility
ETH	Swiss Federal Institute of Technology
FB	Feedback (electronics)
FEM	Finite Element Model
HP3	Heat Flow and Physical Properties Package
InSight	Interior Exploration using Seismic Investigations, Geodesy and Heat Transport
IPGP	Institut de Physique du Globe de Paris
ISAE	Institut Supérieur de l'Aéronautique et de l'Espace
JPL	Jet Propulsion Laboratory
LES	Large Eddy Simulations
LVL	The leveling mechanism for SEIS
MAG	Magnetometer
MPF	Mars Path Finder
MPS	Max Planck Institute for Solar System Research
POS	Position (referring to the seismometer output)
RISE	Rotation and Interior Structure Experiment
RWEB	Thermal blanket for SEIS
SA	The seismometer Sensor Assembly
SEIS	Seismic Experiment for Interior Structure
SP	Short Period sensor
SPHERE	Gold coated evacuated container
TETHER	Electrical cable connecting SEIS to the lander
TTB	Tether storage box
TWINS	Wind sensor
VBB	Very Broad Band sensor
VEL	Velocity (referring to the seismometer output)
VL1	Viking Lander 1
VL2	Viking Lander 2
WTS	Wind and Thermal Shield

⁵ Rutherford Appleton Laboratory, Science and Technology Facilities Council, Didcot, OX11 0QX, UK

⁶ <http://seis-insight.eu/teamlist>

1 Introduction

1.1 The InSight Mission

InSight (Interior Exploration using Seismic Investigations, Geodesy and Heat Transport) is a NASA Discovery Program mission that was selected in 2012. It will place a single geophysical lander on Mars to study its deep interior structure and processes. In comparison with the other missions of the Mars exploration program, InSight is more than a Mars mission—it is focused on understanding the processes that shaped the rocky planets of the inner solar system, and to help establish the comparison between what is known so far (namely from the Earth and the Moon) and what remains to be known: Mars.

InSight will be the first geophysical mission on Mars since the Viking era, and will try to detect the remaining “vital” signs of the planet, deep beneath the surface of Mars. It will embark a complete suite of geophysical instruments: the Seismic Experiment for Interior Structure (SEIS), provided by the French Space Agency (CNES), with the participation of the Institut de Physique du Globe de Paris (IPGP), the Swiss Federal Institute of Technology (ETH), the Max Planck Institute for Solar System Research (MPS), The Imperial College of London (IC), Institut Supérieur de l’Aéronautique et de l’Espace (ISAE) and the Jet Propulsion Laboratory (JPL); and the Heat Flow and Physical Properties Package (HP3), provided by the German Space Agency (DLR). In addition, the Rotation and Interior Structure Experiment (RISE), led by JPL, will use the spacecraft communication system to provide precise measurements of the planet’s rotation.

A suite of other environment sensors (Auxiliary Payload Sensor Suite, APSS) will complement the measurements, helping to understand the environmental impacts on the seismometer: it includes a magnetometer (MAG), a pressure sensor, and a wind sensor (TWINS). A radiometer located on the deck will complement the heat flux measurement. Magnetometer and pressure sensors are key for the system performance, as they are used to decorrelate the seismic signal from environmental contributions. The wind sensor is not used for performance decorrelation, but to discriminate seismic events from wind gusts.

The design of the InSight mission makes use of the same spacecraft that the Phoenix mission used successfully in 2007 to study the icy environment of the northern plains of Mars. Reusing this technology has allowed the team to focus on the challenges of getting the highly innovative instrument suite to Mars.

1.2 SEIS Instrument Overview

The SEIS instrument, see Mimoun et al. (2012), De Raucourt et al. (2012), Lognonné and Johnson (2015) is a *hybrid three-axes* seismic instrument. It is composed of a Sensor Assembly (SA) deployed on the ground, and connected to the instrument electronic box located in the spacecraft (*E-Box*) by an electrical cable referred to as the tether. The SA includes three very-broad-band (*VBB*) seismic sensor heads in an evacuated sphere, three short-period (*SP*) sensors, a leveling system (*LVL*) and a Thermal Blanket (*RWEB*). In order to protect it from the external environment, the SA is covered by a wind and thermal shield (*WTS*). Other SEIS subsystems include a Tether Storage Box (*TSB*) and a cradle to attach the SA on the deck during the cruise. This instrument is resulting from decade of development made mostly by IPGP for the long periods and JPL/IC for the short periods, with a precursor instrument launched on board the failed Mars96 mission—see Mimoun et al. (2012)—and prototypes developed in the frame of the MarsNet/InterMarsnet—see Lognonné et al. (1996) and Net-lander projects Lognonné et al. (2000).

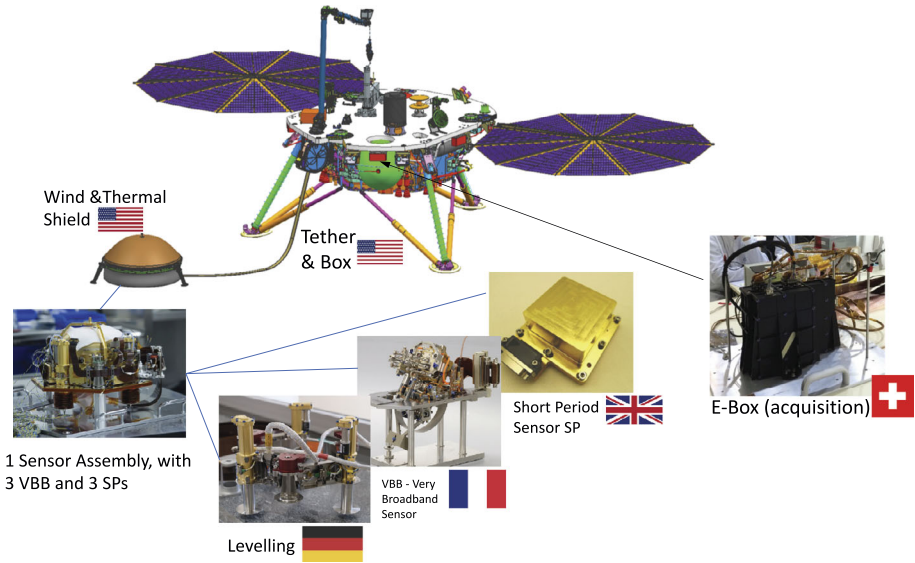


Fig. 1 SEIS subsystems description

2 The Need of a Noise Model for InSight

The precise understanding of an integrated noise model for Mars long-period seismometers, and the derivation of a signal-to-noise study for seismic analysis is a relatively new idea. The evaluation of Martian quake amplitude can, however, be traced to the analysis of the Viking experiment results like Goins and Lazarewicz (1979) that conclude that no seismic event in the Viking seismometer data has been detected, and that seismic events should be hidden by the wind noise. The design of the InSight mission has taken this heritage into account from its very beginning, by deploying the seismometer on the ground, covering it with a windshield, and starting an early analysis of the various noise sources potentially masking seismic events (this work).

In the literature, seismometer noise analysis is often restricted to the self-noise understanding, such as in Ringler and Hutt (2010), as very broadband seismometers normally operate in a seismic vault, in a finely controlled environment, and also because the noise level is limited by the Earth low noise model e.g. Peterson et al. (1993). A good operating environment, such as the Black Forest Observatory deep underground in a mine in Germany, is hundreds of meters below wind and pressure noise sources and has temperature variations of <5 mK, e.g. Kroner (2016). The SEIS seismometer has to operate on the surface of Mars with daily temperature variations of 80 K and highly variable wind and atmospheric pressure conditions. In the challenging environment of the InSight mission, the overarching question is: how can we be sure that the SEIS instrument will operate correctly and measure the seismic events on Mars?

When considering long-period seismograms, there are three main categories of noise: internal sensor noise, environment/installation characteristics that generate noise in the sensor, and seismic noise (see Fig. 2).

Internal sensor noise in a force-feedback seismometer such as SEIS comes mostly from the feedback electronics design. Due to sensitivity to the electronics components' properties and performance, each long-period seismometer has its own characteristics and often quality

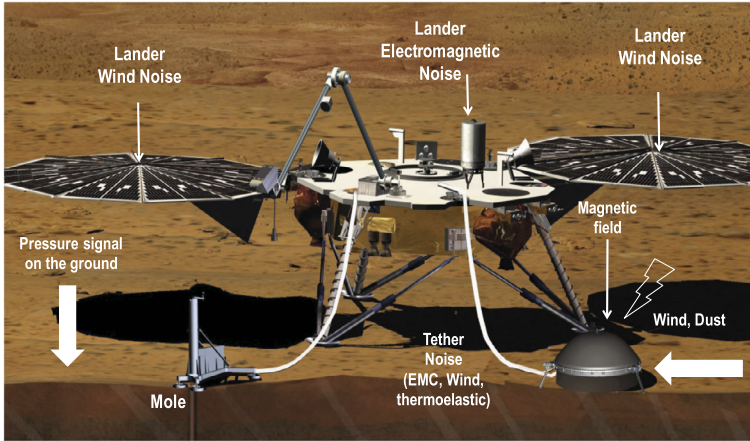
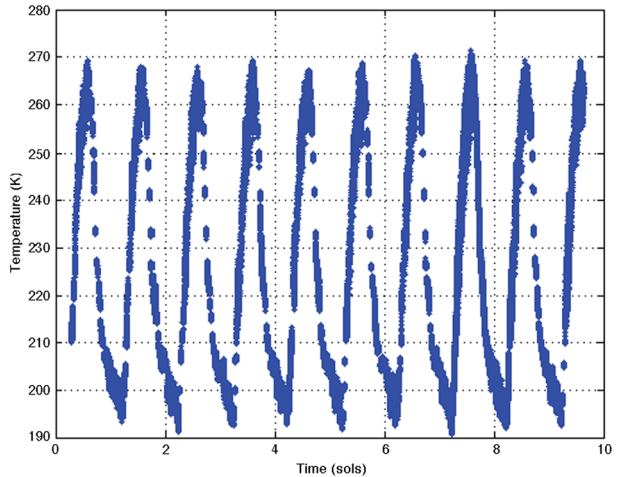


Fig. 2 Environment noise summary

Fig. 3 SEIS is deployed in a challenging environment. External temperature variations on Mars as measured by Mars Path Finder (sols 18–27). Data obtained from the Planetary Data Server



variations can change the performance between different instruments of the same model sensor as described in Ringler et al. (2014). The sensor self-noise is therefore often given by providers as a general shape with intrinsic variability, e.g. in Peterson (1993a,b).

There is a common saying among seismologists that a long-period seismometer is as good as its installation. This highlights the importance of attention to the installation and the minimization of environmental variability in achieving a low-noise long-period seismometer station. Long-period seismometers are usually installed in a dedicated vault, below ground, with very stable environmental conditions. These environmental parameters include the thermal stability of the vault, the barometric stability, (some very long-period seismic vaults are decoupled from external pressure variations with air locks) as well as other important considerations such as the coupling with the ground. Some seismologists recommend installation in a sand box, others on bedrock or on a concrete slab, like in Arias et al. (2014). The quality of the installation also depends on the accommodation of the electrical cable be-

tween the sensor part and the acquisition electronics, and of the shielding from any possible EMC perturbation and of nearby anthropogenic noise, see Peterson (1993b).

The final noise source can be caused by local heterogeneity in the environment and sub-surface. These local effects include ground tilt due to the propagation of pressure waves—see e.g. Murdoch et al. (2016a) or wind acting on local trees coupling into seismic noise. Local topography or complex local geology can cause incident waves to refract and reflect, adding complexity to the seismograms.

It is often difficult to distinguish between the noise of the instrument itself (its electronics) and the noise of its installation, and the noise of the instrument in its environment (for example a contribution due to the thermal sensitivity of its various components).

The general approach followed for Earth long-period seismometer setup is therefore to install the seismometer, to mitigate the known sources of noise of the installation, to record the environment noise specific to the installation and to adjust the installation in order to lower the overall noise in a more or less empirical way: for instance, by putting the installation on sand, or by forming one or more loops around the seismometer with the tether as described in Forbinger (2012). Such an empirical installation procedure cannot be applied in our InSight case: the robotic arm deploying the seismometer has a limited capability of manipulation, thus severely limiting possible seismometer setup options. The optimization of the installation will therefore rely on a quantitative estimate of the seismometer and its installation noise in the possible deployed configurations.

A quantitative approach for estimating the performance of the SEIS seismometer on Mars needs the following steps:

1. Build a noise model which identifies all possible contributors, measure the instrument self noise, measure the instrument sensitivity to the external environment and build a complete noise estimate of the instrument in the Martian environment.
2. Follow the performance maturation during the mission design and development: during the mission design process, various parts of the system change their performance, from estimated values to measured and validated values. The noise model allows the effect of the performance evolution to be tracked through the mission design and development process.

Of course, once SEIS installed on Mars, the proposed noise model will be updated to reflect the actual mission performance in its environment.

3 The Noise Map Approach

3.1 Listing the Various Contributors to the Noise Analysis

Constructing a noise model requires a painstaking identification and evaluation of every potential noise contributor. Of course, particular attention has been paid to identify dominant noise sources. There are three broad categories of noise sources (see Fig. 2):

1. Instrument Noise (Self-noise): includes contributions from sensor head, electronics and tether.
2. Environmental effects generating noise in the instrument (thermal sensitivity impact, magnetic field impact, thermoelastics...).
3. Environmental effects generating ground acceleration (pressure signal, wind).

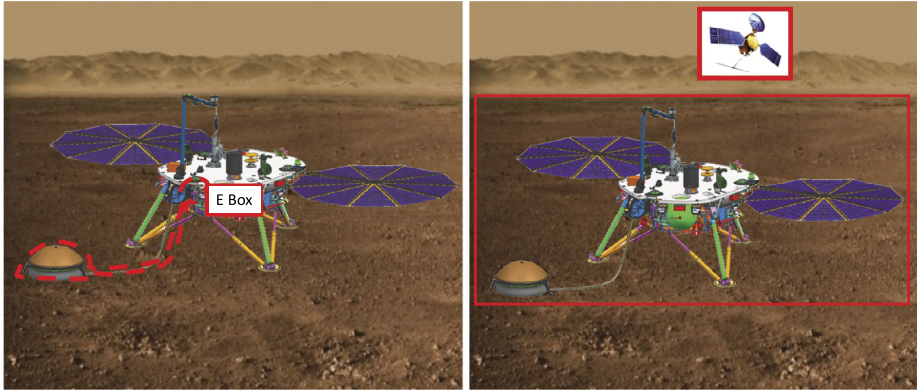


Fig. 4 (Left): L4 errors contributors are related to contributors within the red line (at SEIS instrument level) Mitigation of noise sources are at Instrument level—(Right): L3 errors contributors are related to contributors within the red line (Payload and mission system level errors)

Finally, it is also possible to use a more “classical” noise analysis, which includes the evaluation of noise sources at various levels of the measurement chain transfer function. However, none of these approaches help us to map the various noise sources in order to prevent us from forgetting a key element of the model. We have therefore chosen a third approach: trying to “map” the various noise sources as a matrix (see Fig. 6) including the various parts of the system as well as the potential environmental noise sources.

In this paper, we have chosen to label as “self-noise” or “instrument noise” all the contributors due to the instrument itself (all noise sources originating from a location within an imaginary line around the instrument) or to its thermal sensitivity (see Fig. 4). Note that all seismic performances related to the instrument are called “L4 requirements” in the project typology that we use in this paper for the sake of consistency (see Fig. 5). We have labeled as “system” noise all noise sources where the system (understood as the seismometer plus the spacecraft with the same imaginary line drawn around the two) has a contribution. This includes electronic perturbations coming from the lander, and pressure induced ground tilt and acceleration; but also includes external noise sources that we try to partially decorrelate or mitigate. All performance requirements related to these InSight system aspects are called “L3 requirements” in the project typology.

3.2 The InSight Noise Map

The noise map (Fig. 6) is a helpful tool in order to map a summary of all possible noise components with an impact on the system. The columns of the noise map correspond to the various instrument subsystems (VBB, SP, SPHERE, LVL, acquisition, tether. . .), and the rows of the noise map corresponds to the environmental parameters (temperature, wind, dust pressure. . .). As an example, the (SPHERE, temperature) couple, identifies two possible contributions: thermal noise on the instrument and sphere thermoelastic noise.

Computations of each of the identified contributors’ noise amplitude have been added (see next sections), and compared to the VBB self-noise preliminary estimate (which was around $10^{-9} \text{ m/s}^2/\sqrt{\text{Hz}}$ in the [0.01–1] Hz bandwidth). Noise components are then classified along the following categories: noise components which are negligible with respect to the preliminary estimates (<10% of total noise) and dominant noise components (>10% of total noise).

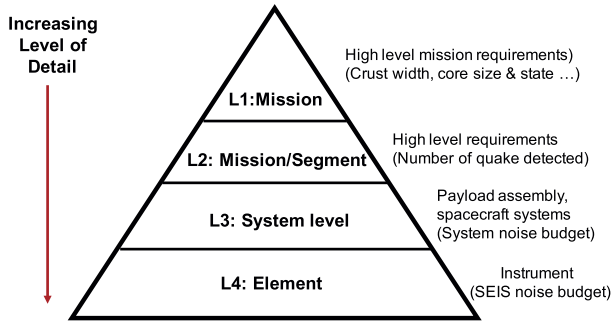


Fig. 5 Architecture of the mission requirements. Mission requirements are expressed at L1 and L2 levels, and are flowed-down to L3 level (payload assembly performance). The instrument requirements related to SEIS (L4) requirements are flowed-down from L3 requirements. Therefore instrument (L4) requirements include all instruments contributions. InSight System related noise (L3) include all contributors originating within a red line/surface enclosing the InSight lander

	Self noise and environment impact on Sensors		Acceleration Noise Contributors				Post-detection Noise Contributors	
	SPHERE	SP	LVL	WTS	Lander	TTH	E-box	S/W
Self generated	VBB Self Noise	SP Self Noise			EMC Noise	Crosstalk (included in self noise)	Acquisition Noise	Data Processing
Temperature	Thermal noise Thermoelastic	Temp Sensitivity	Thermoelastic Sensitivity (tilt)	Included in Sphere Calc.		Thermoelastic noise	Included in Acq. Noise	
Wind	Residual Wind			Mechanical Noise (tilt)	Lander Motion (Inc. Solar Arrays)	Mechanical Noise		
Dust				Saltation		Saltation		Significant Source
Pressure	Buoyancy Grav. Attr.		Ground Tilt					Significant Source decorrelated
Mag. Field	External Magnetic field				Lander			Minor (< 0.1 x Req)
Sun Radiation				Incl. in Sphere T Calc.	Incl. in Sphere T Calc.	Incl. in Tether temperature		

Fig. 6 Noise map outline—three types of errors are depicted here: errors which are a significant part of the total error budget (*brown*, >10% of total noise), minor sources of errors (*green*, <10% of total noise), errors which are a significant part of the error budget but will be decorrelated by auxiliary sensors (*dashed green-brown*)

Early estimates of the pressure such as Lognonné and Mosser (1993) and of the magnetic noise levels have indicated that their contribution could hide a large number of seismic events, and may possibly impede the ability to detect faint seismic signals. In order to be able to remove the contribution of the signal directly related to environmental variations (and increase the useful seismic signal-to-noise ratio), an Auxiliary Payload Sensor Suite (APSS), which consists of wind, temperature, pressure, and magnetic field sensors auxiliary sensors has been implemented on the mission. A pressure sensor (microbarometer) and a

Table 2 Noise requirements for instrument and system

Axis	Bandwidth	Instrument requirement	System requirement
Horizontal	[0.1 1] Hz	$10^{-9} \text{ m/s}^2/\sqrt{\text{Hz}}$	$2.5 \times 10^{-9} \text{ m/s}^2/\sqrt{\text{Hz}}$
Vertical	[0.01 1] Hz	$10^{-9} \text{ m/s}^2/\sqrt{\text{Hz}}$	$2.5 \times 10^{-9} \text{ m/s}^2/\sqrt{\text{Hz}}$

magnetometer will partially remove the associated noise contributions leaving only a small remainder of the noise component which cannot be removed (see Sects. 5.9 and 5.7) in the noise budget. The theoretical background for pressure decorrelation can be found in Murdoch et al. (2016a).

4 Variability of the Noise Model and Associated Requirements

4.1 Environment Variability Modeling

As described in Sect. 2, one of the key assumptions that we made is that environment-related noise spectra are proportional to the related environment spectra multiplied by the instrument sensitivity. As an example, we assume, and this is a worst-case approach, that the thermal noise is derived from the temperature spectrum by a scale factor, which is constant over the seismic bandwidth, the temperature sensitivity. Therefore, we have also chosen not to consider also a worst-case approach on the various environmental parameters we are using: it would lead to non-realistic worst case noise estimates for the seismometer and it would constrain the InSight mission design in an irrelevant way.

The general assumption made for the InSight performances is that 70% of the time, background noise will be within typical values: we have assumed that environment parameter distributions are close enough to normal distributions to be able to consider that about 70% and 99.7% of the time-dependent environmental parameters (e.g. temperature, wind as a function of time) lie within one and three standard deviations of their mean (1σ and 3σ).

The details on the calculation of the environment parameters profiles are described in Appendix B. As an example, we have used Martian temperature spectra derived from Viking and Mars Path Finder data (see Sect. B.5 for more details). Another example focusing on the wind speed estimations can be found in Murdoch et al. (2016b).

In addition, the environment variability is important: we have chosen to split the sol (Martian Day) in two arbitrary periods “day” and “night”. “Day” corresponds to the local hours between 6:00 AM and 6:00 PM, and “night” corresponds to 6 PM and 6 AM.

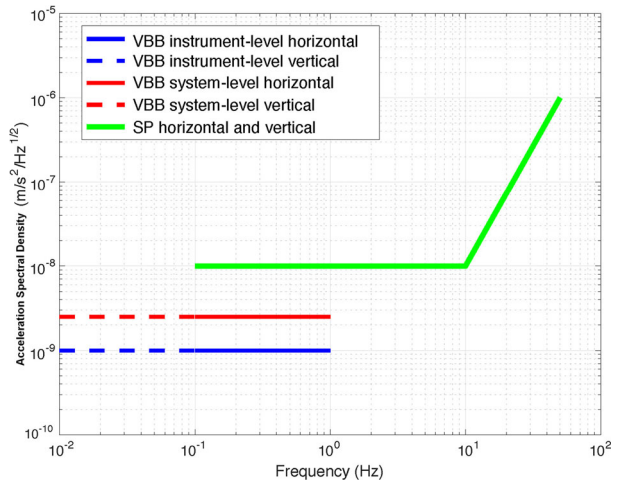
4.2 Noise Requirements

The noise requirements have been defined to allow the system to detect a sufficient number of quakes during the operational life of the lander (1 Mars year, 2 Earth years). They are presented in Table 2 and Fig. 7. These noises are specified at instrument (L4) and system (L3) levels, on both vertical and horizontal axes. Note that the horizontal requirements extend down to 0.1 Hz and vertical axis requirements extend to 0.01 Hz.

4.3 Noise Requirements Discussion

The noise requirements that have been used in the InSight mission design are related to the maximization of the various quake waveform detection—see Panning et al. (2015), Khan

Fig. 7 InSight performance requirements. The *dashed lines* apply only to the VBB vertical, while the *solid lines* apply to both horizontal and vertical components. Horizontal requirement envelope is reduced due to the tilt impact of several noise sources. In *red*, system requirements. In *blue* and *green*, instrument related requirements



et al. (2016), but they are also based on a bottom-up approach, with an instrument and the system performance being the main driver for the scientific return. The horizontal requirements do extend only down to 0.1 Hz: this is linked to the impact of the tilt noise. At low frequency, any tilt of the instrument (due to the intrinsic deformation or due to external cause) is seen as an acceleration. If α is a tilt and g_0 the local gravity vector, then any instrument will measure $g_0 \sin \alpha$ on the horizontal axis. It is worth noticing that some seismic signals (as the tilt due to the pressure field) are also accounted as system noise, for two main reasons:

- First, the pressure noise affects the instrument noise floor over most of the bandwidth. It can therefore contribute to masking remote quakes waveforms, and deemed as “noise” in the signal to noise ratio analysis.
- Secondly, a barometer has been implemented to help mitigate this sizing contribution. The overall system performance will strongly depend on the quality of the decorrelation of this pressure signal by the micro-barometer (this is a system performance) and of the micro-barometer performance.

This is also true for the magnetic noise.

4.4 Noise Budget Tables

Major (>10%) instrument noise error contributions from the noise map (L4) are described in Table 3. This table is the one used to track the system performance budgets. Minor (<10%) contributions are not presented here. They are detailed in Appendix A.

5 Noise Related to the Instrument

5.1 Very Broadband Sensor (VBB) Performance

The VBB self-noise sensor performance is at the heart of the overall system performance. As the VBB is operated on Mars, under Mars gravity, the contribution to the overall noise performance of the VBB is a composite noise, derived from Earth performance measurements and theoretical considerations.

Table 3 Expected noise sources table

Major noise sources	Description
<i>Instrument noise</i>	
Self noise	Instrument self-noise
Thermal noise	Temperature impact on instrument
Thermoelastic tilt	Instrument distortion under thermal stress
Tether dilatation	Impact of tether thermal stresses on sensor assembly
Heaters	Thermoelastic resulting from switch on of heaters
Acquisition	E-box acquisition noise
Wind on WTS	Tilt on the instrument resulting from wind stresses
<i>System noise</i>	
Wind on lander noise	Impact of the lander motion
Wind on HP3	Impact of the companion payload HP3
Lander EMC noise	Lander radiation
Magnetic noise	Magnetic field impact (will be decorrelated)
Pressure noise	Pressure noise (will be decorrelated)

5.1.1 Very Broadband Sensor (VBB) Description

The VBB is a closed loop system, where an inverted mechanical pendulum is locked onto its mean position by a magnetic force feedback. Its sensitivity axis is inclined at 30 deg with respect to the horizontal axis. The three VBB sensitivity axes (U , V , W) can be recombined to yield the ground motion in the (X , Y , Z) coordinate frame. Two feedback have been implemented: a “Science” feedback, which optimizes the scientific performance, and a more robust “Engineering” feedback, which is primarily used to recenter the proof mass. As a result of this design, the main contributors of the self-noise are the suspension noise (Brownian noise), the displacement transducer (Differential Capacitive Sensor = DCS) noise, the coil actuator noise (Johnson noise) and the analog feedback noise. The analog feedback noise is composed of various contributions from its parts: operational amplifiers, resistors and capacitors—see Mimoun et al. (2007) and has been provided by the VBB project team (Nebut T., O. Robert et al., personal communication). This VBB noise model has been validated by several tests at subsystem levels.

5.1.2 Very Broadband Sensor (VBB) Feedback and Noise

The science feedback electronics uses two proportional derivative-like feedback, and has two outputs: one proportional to the velocity of the ground (called the VEL output) and another proportional to the ground displacement (called the POS output) (see Fig. 8). Each of these outputs has its own noise level, but the overall output performance is linked to the minimum of the noise for a given frequency of these two outputs (see Fig. 9). A typical analysis of seismometer self noise can be found in Sutton and Latham (1964). As the VBB sensors are only balanced in Martian gravity, VBB self-noise with respect to its own direction of sensitivity (at 30 deg with respect to the horizontal axis) is first evaluated in a terrestrial environment and then scaled to represent the more correct (and more favorable) Martian gravity. The resulting figures are then rotated to reconstruct the vertical axis noise.

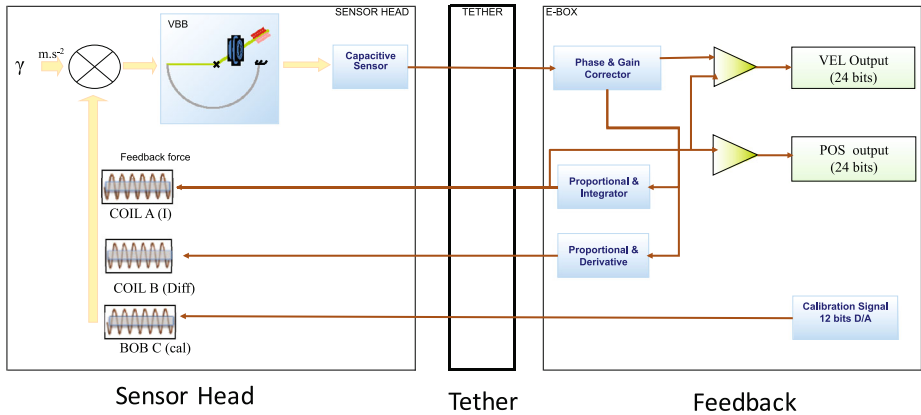
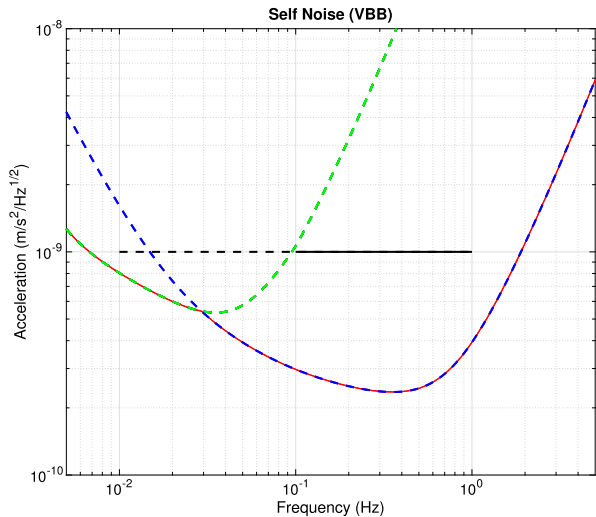


Fig. 8 Very Broadband Sensor schematics. On the *left* a schematics describing the VBB sensor, including its pendulum, the Differential Capacitive Sensor (DCS) and the three coils. On the *left* an overview of its analog feedback with its two outputs: velocity (VEL) and position (POS)

Fig. 9 VBB sensor head self-noise performance. In *dashed blue* the noise of the VEL (Velocity) output. In *dashed green* the noise of the POS (position) output. In *red*, the best noise achievable from the sensor. In plain and *dashed black lines*, the instrument level requirement. The vertical requirement extends down to 0.01 Hz, while the horizontal extends only to 0.1 Hz. NB: This VBB noise level is achieved in the sensor sensitivity axis, inclined from 30 deg from horizontal



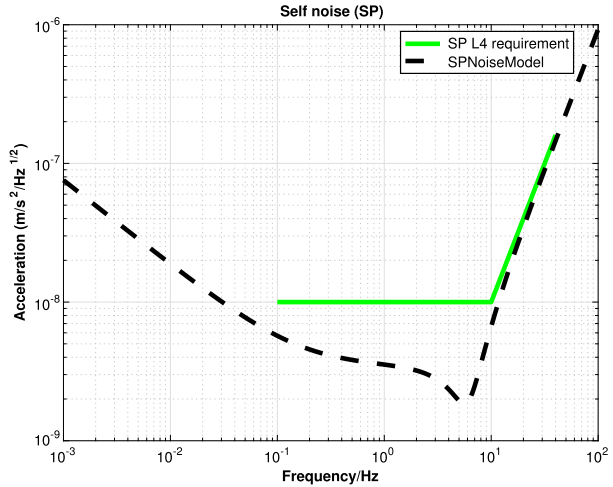
This is done by using a rotation matrix to go from the $U-V-W$ physical axes of the three VBB sensors to the $X-Y-Z$ instrument main reference frame.

The sensing element of SEIS is located on the Martian ground, its electronics (the feedback loop) is protected inside the lander and encounters the thermal excursion of the lander warm box. We discuss in Appendix A.1 the thermal sensitivity of the VBB feedback. This is a minor contributor to the instrument noise.

5.1.3 Limitations of the VBB Noise Model

Of course, the VBB noise model is only a “theoretical model” that accounts for main contributors. Depending on the perturbation in the environment, and given the fact that VBBs are not fully functional on Earth—they are adapted to Martian gravity—performance measurement can be limited by measurement setup, clean room installations, and noise assess-

Fig. 10 The SP noise (*black dashed*) model taking into account the suspension noise, the amplification noise and the ADC noise. Also shown *in green* is the SP L4 requirement



ment methods, which can be only as good as the reference sensors used—see e.g. Ringler et al. (2014). At the limit of performance that we reach (below $10^{-9} \text{ m/s}^2/\sqrt{\text{Hz}}$), it is often difficult to discriminate between self-noise, environmental perturbations and mathematical artefacts to data processing (sampling, synchronization. . .)

5.2 Short Period Sensor (SP) Performance

The SP sensors (one for each X , Y , Z axes) are mounted on the LVL ring, with an SP sensor above each LVL leg. This is different from the VBB sensors which are mounted at the central point within the ring (see Fig. 1). The major noise sources for the SP are the suspension noise, the noise from the preamplifier of the displacement transducer, and a flicker noise generated within the sensor itself.

The noise contributions from the suspension can be modeled directly from the thermodynamic considerations as having an acceleration noise density of $\sqrt{\frac{kT\alpha}{m}}$, where k is Boltzmann’s constant, T , the absolute temperature, α , the damping constant of the suspension and m the proof mass. Unlike the VBB, the SP is not maintained at a high vacuum, to reduce α but is in a controlled nitrogen atmosphere at Mars pressure to reduce α . The damping is set by the viscous Couette flow in the $12 \mu\text{m}$ gap of the displacement transducer, and this gives a white noise floor for the SP’s 0.8 g proof mass of about $2.10^{-10} \text{ m/s}^2/\sqrt{\text{Hz}}$.

The differential preamplifier of the displacement transducer introduces the second contribution from its input voltage noise. This is equivalent to a $10^{-12} \text{ m}/\sqrt{\text{Hz}}$ displacement noise, which for the 6 Hz suspension of the SP produces a noise floor below resonance of $2.10^{-10} \text{ m/s}^2/\sqrt{\text{Hz}}$, rising as $1/f^2$ above resonance.

The third, flicker-noise contribution is determined empirically from noise testing which is performed using conventional coherence techniques, with the vertical axis of the SP tilted to simulate the reduced Mars gravity. Figure 10 shows both the contributions and noise floor for one of the flight-model SPs from testing on the flight model (FM) system. The additional contributions apparent from LVL, the tether, or the acquisition electronics are similar to those of the VBB.

5.3 Thermal Noise Modeling

Both VBB and SP sensors are sensitive to the temperature fluctuations: the output of the sensor includes a thermal “signal” derived from the temperature that can be detected on the horizontal and vertical axes. The complete modeling of this temperature is complex: the change of pendulum temperature results in a change in geometric properties of the sensing elements (due to thermoelastic effects). This results in the change of the pendulum equilibrium position, which is seen as a parasitic acceleration. This parasitic acceleration can be seen at all frequencies of the sensor, from diurnal variation (which may result in a possible saturation of the sensor) to short term variations measured in the sensor seismic bandwidth. Given the harsh thermal environment on Mars—see Fig. 3, thermal noise is one of the dominant noise sources on the system, especially at long period, which requested the integration of efficient thermal protection in the design.

In order to reduce this noise, and to avoid saturation of the instrument under the effect of such thermal excursion, passive and active measures have been implemented. First, the VBBs and the SPs are each protected by three layers of insulation: the WTS, the RWEB and a gold coated evacuated container (the “sphere”) for the VBBs, and the WTS, the RWEB and the SP-box for the SPs. Note that this concept of wind shielded protection, already suggested by Anderson et al. (1977) following the Experience Return of Viking, was very rapidly tested (e.g. Lognonné et al. (1996) for wind shield tests made for InterMarsnet). For OPTIMISM on Mars 96, this was made by the Small Station itself, see Linkin et al. (1998).

The second device is active: the VBB includes a device allowing the displacement of a small mass as a function of the temperature which compensates for the equilibrium motion. The excursion range of this small mass can be tuned by the rotation of a Temperature Compensation Motor or TCM.

The noise model includes a first order temperature sensitivity approximation, where the sensors’ outputs are proportional to the temperature variations (“thermal sensitivity” in $m/s^2/\sqrt{(Hz)/K}$). The VBB thermal sensitivity can change depending on the TCM position.

The thermal wave propagation has been also simplified: we assume that the WTS, the sphere and the SP-box act separately as first order thermal filters between their external interface and their internal interface. As a consequence, the temperature spectrum seen by the sensors is the convolution of the two first order $\frac{1}{1+\tau p}$ filters, where p is the Laplace transform variable, τ is the filter time constant: the wind and thermal shield plus the RWEB and the sphere for the VBBs, and the wind and thermal shield plus the RWEB and the SP-box for the SPs. The values for the first order filter thermal constant (τ) of the WTS, of the sphere and of the SP box have been measured during thermal vacuum tests: “Wind and Thermal shield” time constant is 7.2 hours, “Sphere” 3 hours and SP box 460 seconds, respectively. The temperature spectrum before and after filtering is depicted at various locations of SEIS is shown in Fig. 11. The resulting thermal noise, depending on day and night profiles, is shown in Fig. 12.

Thermal sensitivity has been directly measured on all VBBs. The uncompensated thermal sensitivity (i.e. without TCM activation) shows higher values than expected as well as a dependency upon temperature; therefore the optimal position of the thermal compensator will change with the season. The SP thermal sensitivity has been measured in the laboratory tests using the sensor mass position and the Mars best current estimate is determined by extrapolating these results to the Martian gravitational environment.

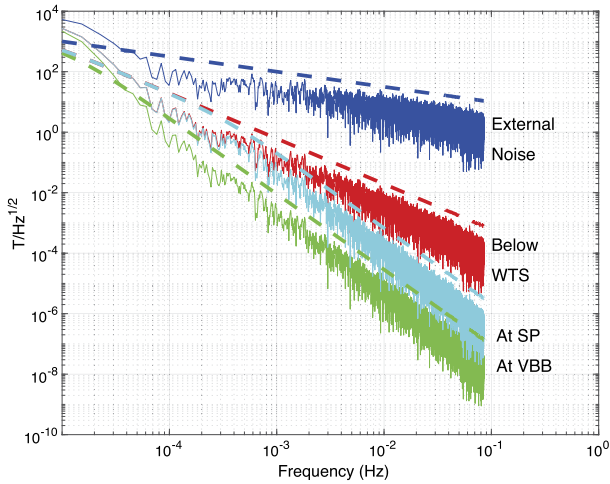


Fig. 11 Thermal variations spectrum: external temperature variations and linear temperature model (*blue solid and blue dashed*), external temperature variations and linear temperature model filtered by the WTS only (*red solid and red dashed*), external temperature variations and linear temperature model filtered by both the WTS and the sphere (*green solid and green dashed*), external temperature variations and linear temperature model filtered by both the WTS and the SP box (*cyan solid and cyan dashed*). The values for the first order filter thermal constant of the WTS, the sphere and the SP box have been measured and are 7.2 hours, 3 hours and 460 seconds, respectively. The rupture in the slope corresponds to the WTS and sphere thermal filter cut-off frequencies. A full description of the thermal profiles used is provided in Appendix B.5

5.4 Thermoelastic Tilt

The thermoelastic tilt (see Fig. 15) is the resulting signal measured by the seismometer due to an inhomogeneous temperature distribution over the instrument, or inhomogeneous thermal expansion coefficient (CTE) of its components: when a part of the instrument has a change in dilatation which is not homothetic, this results in a tilt, detected as noise on the horizontal axis. As a result of the external temperature variations, the various parts of the instrument experience inhomogeneous thermoelastic expansion/contraction cycles.

The analytical model that we developed was initially based on the estimation of various subsystem contributors to the total thermoelastic tilt: tilt induced by the homogeneous dilation of the sphere and its ring, tilt induced by heterogeneous and differential dilation of the sphere/ring assembly, and tilt induced by the heterogeneous and differential dilation of the LVL legs. This has since been replaced by a simpler model with one overall thermoelastic tilt sensitivity derived from a finite element modeling (FEM). The chosen approach was to determine the worst case of thermoelastic tilt for all SEIS deployment configurations.

Once the analysis is done, the thermoelastic tilt is evaluated for each configuration. (Described in Fig. 13.) A statistical repartition of these values is presented in Fig. 14.

5.5 Tether Dilatation

The tether noise (see Fig. 18) is another aspect of the thermoelastic impact on the seismometer. Even if its contribution is now negligible, we have chosen to highlight its modeling as it could have been a major contribution to the overall noise budget, mitigated only by the particular attention paid to this issue. The tether noise is potentially one of the most significant noise sources in the baseline design and we know that one of the Apollo seismometers

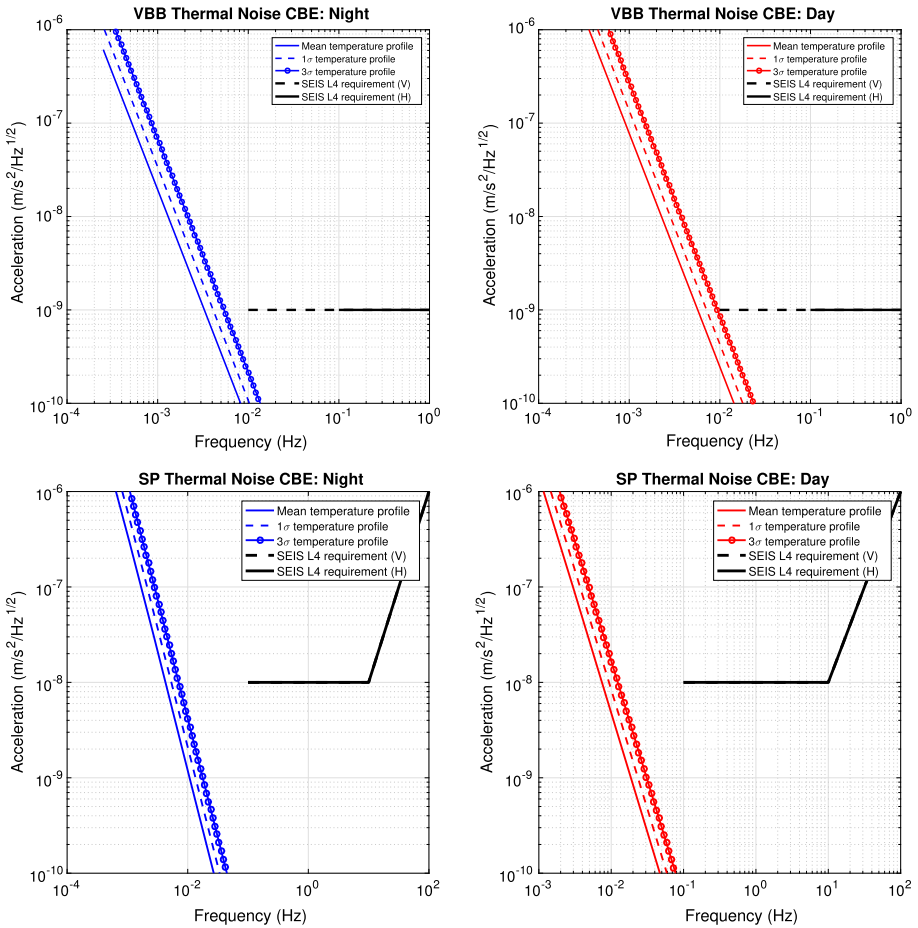


Fig. 12 The estimated vertical thermal noise contribution for the VBBs (*top*) and SPs (*bottom*) during the night (*left*) and day (*right*). The current best estimates of the thermal sensitivities have been used in the noise model. For the vertical, these are $2.3 \times 10^{-5} \text{ m/s}^2/\text{K}$ for the VBBs, and $2.5 \times 10^{-6} \text{ m/s}^2/\text{K}$ for the SPs. The horizontal thermal sensitivities (not shown in this figure) are $3 \times 10^{-5} \text{ m/s}^2/\text{K}$ and $3.5 \times 10^{-6} \text{ m/s}^2/\text{K}$ for the VBBs and SPs, respectively. Increasing values of noise represent mean, 1σ and 3σ noise levels, respectively. The typical thermal noise is assumed to be the 1σ day time values

did not work well due to cable issues—see Lognonné and Johnson (2015). It has therefore been evaluated separately from the other thermoelastic contributors.

The thermal energy from the environment heats the tether causing it to expand or contract and exert a force on the seismometer (Fig. 16). On an Earth seismometer, a “loop” of the cable around the sensor mitigates this force, but with our current design, the tether pushes the seismometer and induces a tilt as the SEIS legs are pushed down into the compliant regolith (Martian ground); this motion is indistinguishable from a seismic signal. The material of the tether that is changing dimension/imposing strain is primarily copper, which is used for the traces conducting the signal between the E-Box and the sensor head, and ground planes. The polymer film which composes the insulation of the tether is a secondary or lower-order contributor. In order to mitigate this effect, it has been chosen to fold the tether (“tether shunt”) before its contact to the Surface Assembly (see Fig. 17).

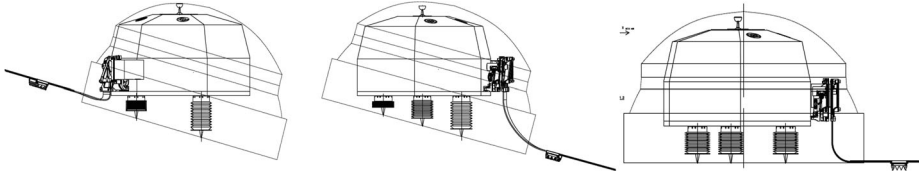
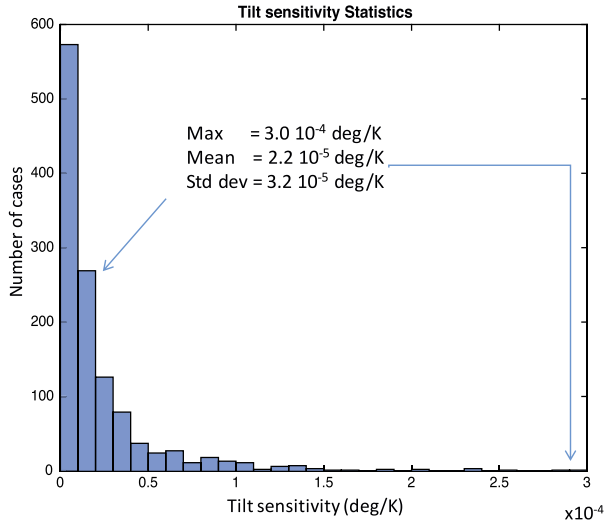


Fig. 13 Schematic of the seismometer deployed on the ground: three examples of the studied deployed SEIS configurations

Fig. 14 Repartition of tilt sensitivities for all SEIS configurations. The 1σ value of tilt sensitivity is considered as reference. Courtesy CNES



We have then used a complete Finite Element Model (FEM) of the seismometer and its attached tether to predict the tilt for a given temperature variation. This static tilt sensitivity, including the protection by the WTS of the last centimetres of the tether, is then translated through the tilt force into a noise contribution.

These simulations (see Fig. 17 for the FEM model description) show that the tether, in the deployed configuration, does not induce a tilt sensitivity in the seismometer greater than 10^{-11} rad/K for thermal variations in the atmosphere outside the WTS. We assume a ground stiffness of 10^6 N/m, which is far below our measurement capabilities. Ground tests performed by CNES in order to check these performances were not able to detect bigger effects.

5.6 Acquisition Noise

The acquisition noise has been designed to remain below the self-noise (see Fig. 19). It has been measured and is linked to the Analogue to Digital Converter (ADC) performance. Its contribution is generally negligible in the bandwidth where the VBBs or the SPs have high gains. It can be a significant source of noise at short periods above 5 Hz for the SP, and is one of the major sources for the low gain mode of the VBB, e.g. POS LG.

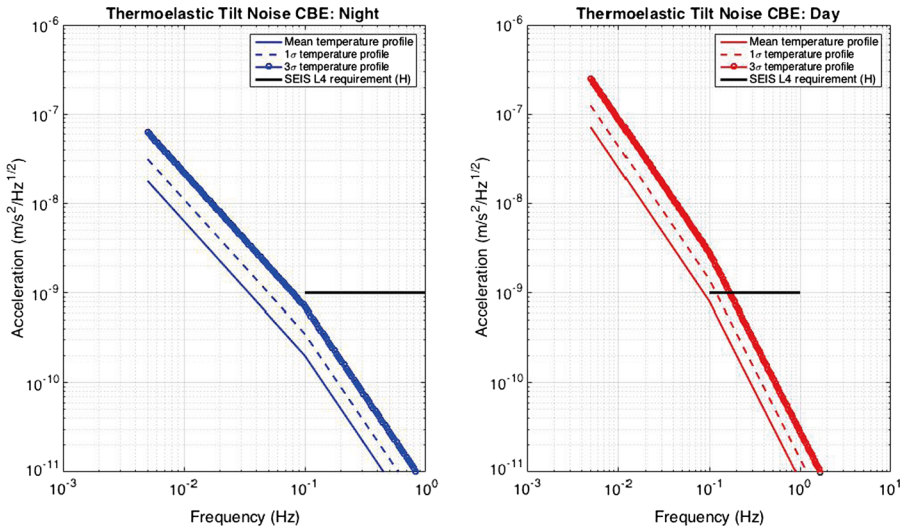


Fig. 15 Overall thermoelastic tilt of the instrument. We assume a 5.4×10^{-5} deg/K overall thermal sensitivity of the instrument. Increasing values of noise represent mean, 1σ and 3σ noise respectively—Typical Noise is 1σ

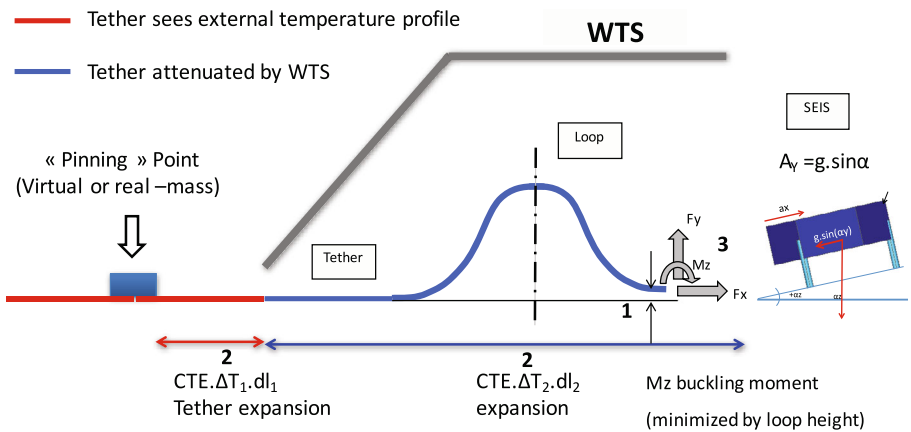


Fig. 16 Impact of tether thermoelastic on SEIS

5.7 Magnetic Noise

5.7.1 Magnetic Noise Sensitivity

The VBB sensor is sensitive to magnetic field fluctuations; this is due to the material of the pendulum spring, which is made of a magnetic alloy. For a general description of the phenomenon, see e.g. Forbriger et al. (2010). Any magnetic field fluctuation creates a torque on the pendulum (the VBB has a magnetic moment \vec{M}) which creates a magnetic noise that will be detected by SEIS (see Fig. 20). The SP, being made of silicon, is not sensitive to magnetic fluctuations. The resulting VBB magnetic noise model is, therefore, very simple:

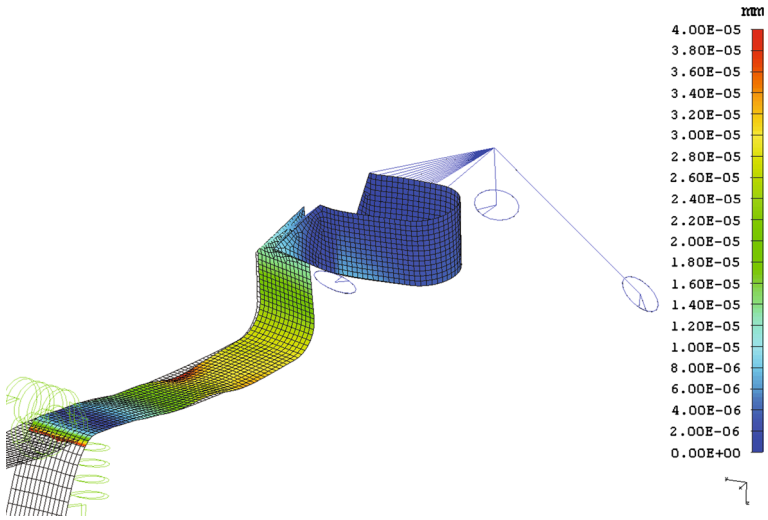


Fig. 17 Tether thermoelastic model on SEIS, used to evaluate tether shunt performance. Tether displacements close to SEIS are subject to thermal input. Tether is supported elastically at pinning mass and SEIS supported elastically at feet. Tilt for SEIS is computed for a static 10 K temperature variation of the tether. Scale on the right is the displacement. Courtesy ATA engineering

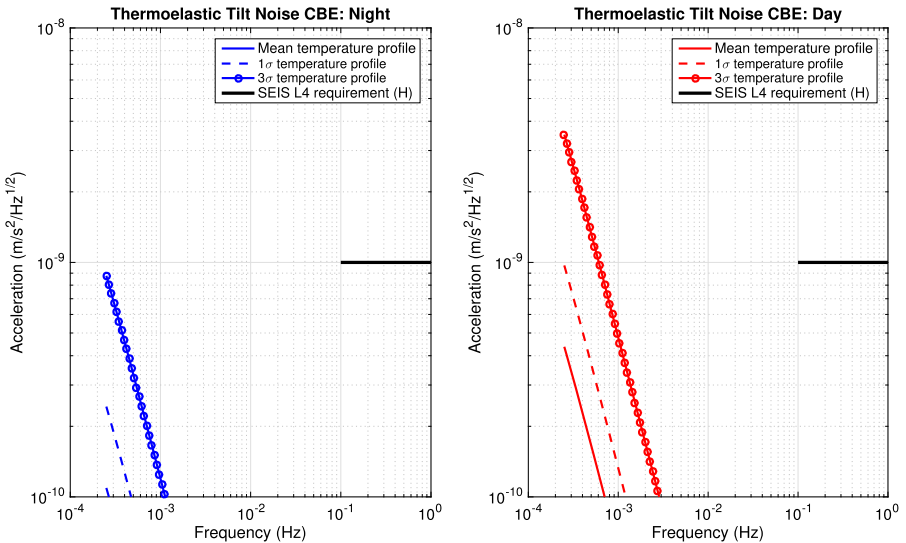
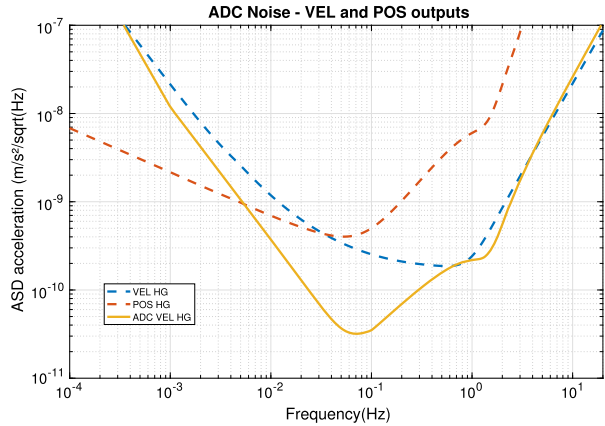


Fig. 18 Tether related tilt noise of the instrument. Thanks to the tether mechanical shunt assembly, tether noise becomes negligible. Increasing values of noise represent mean, 1σ and 3σ noise respectively

the pendulum sees the acceleration $\vec{M} \times \vec{B}$. It is, therefore, possible to derive the magnetic sensitivity of the instrument axis by axis or globally (as done here).

The VBB magnetic sensitivity has been measured for the three VBB axes and data have been filtered between 0.005 and 0.01 Hz. In this frequency band, as predicted by the model, there is a very good correlation between the magnetic signal and seismic signal, allowing

Fig. 19 Acquisition noise—the acquisition noise (yellow line) compared to the reference noise of the instrument for POS and VEL



estimation of the magnetic sensitivity for all VBB sensors. The sensitivities are close to the initial requirements, between $3.5 \times 10^{-10} \text{ m/s}^2/\text{nT}$ and $5.4 \times 10^{-10} \text{ m/s}^2/\text{nT}$.

5.7.2 Magnetic Field Assumptions

If the estimation of the magnetic sensitivity is straightforward, the estimation of the magnetic field on Mars is quite challenging. No magnetic data have ever been recorded at the Mars surface. The issue here is, therefore, to use orbital DC+AC measurements above the ionosphere from Mars orbiters (such as MGS), and extrapolate these data to the AC magnetic field below the ionosphere. This has been done using measurements from several adjacent paths above the same area (equator crossing above Pavonis Mons). The resulting field has been corrected for the crustal (DC) field, and the residual is used as a proxy for the AC magnetic field. We use an updated version of the data presented in Langlais et al. (2004), with contributions from (Johnson et al., 2016, private communication). However these results shall be considered with caution, due to the many uncertainties related to these measurements.

5.7.3 Magnetic Field Decorrelation

The uncertainty of the magnetic field value, and the associated potential high level of magnetic noise, has led the mission to implement a magnetometer as part of the InSight APSS in order to decorrelate the magnetic noise and, thus, to improve the signal-to-noise ratio. The mechanism of the magnetic field perturbation being straightforward, it allows a very efficient decorrelation of the magnetic field contribution. We therefore assume that up to the magnetometer noise level, the contribution of the magnetic field can be reduced to 10% of its potential value. We assume that this decorrelation is limited by the self-noise of the magnetometer.

5.8 Mechanical Wind Noise

The seismic noise induced by the wind on a lander has been the main source of noise witnessed by the Viking seismic experiment—see Anderson et al. (1977), Nakamura and Anderson (1979). As the Viking seismometers were located on the top of the Viking lander platform, it appears—e.g. Goins and Lazarewicz (1979) that during a large fraction of the

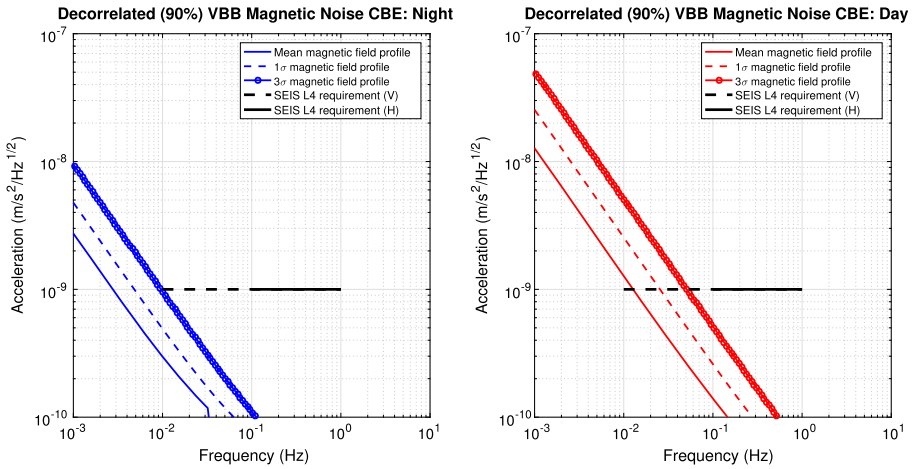


Fig. 20 The estimated vertical magnetic noise contribution. A worst-case VBB vertical magnetic sensitivity of $3.8 \times 10^{-10} \text{ m/s}^2/\text{nT}$ has been considered, as well as a 90% efficiency of the decorrelation up to the magnetometer self-noise, estimated to be $0.3 \text{ nT}/\sqrt{\text{Hz}}$. In *dashed black* and *solid black*, respectively, the expected performance requirements of the SEIS instrument (L4) on vertical and horizontal axes

operational life of the instrument, the seismic measurements were in fact related to the motion of the platform under the wind dynamic pressure. The InSight mission has taken this into account, and the seismometer is now deployed at the surface of Mars by a robotic arm. However, it does not mean that the measurements are not perturbed by the wind: the lander will vibrate under the wind motion, transmitting vibrations through the ground to SEIS. The WTS designed to protect the seismometer from the direct wind, will also induce both a ground tilt and acceleration under the wind pressure. It is also to be noted that the position of the location of the seismometer (close or remote from the lander) also has an impact on the noise level. In the following example, SEIS is deployed at its baseline position (see Fig. 34), but a major output of this study is the capability to predict the noise as a function of the instrument deployed position in a “noise map”. This section makes a summary of the study of the mechanical noise induced by the wind, but a more detailed description can be found in Murdoch et al. (2016b). See Lognonné et al. (1996) for precursor tests on the wind shield efficiency.

The principle for the computation of the mechanical noise contribution of both WTS and lander is similar and described in Fig. 21. Dynamic pressure models are derived from the mean wind statistics described in Fig. 47. At frequencies where measurements are not sufficient (below 100s), wind speed spectral distribution is derived from Large Eddy Simulations (LES) models and theoretical considerations. This dynamic pressure is then used to compute the stresses on the ground resulting from drag and lift of the considered body (InSight Lander and WTS aerodynamic coefficients were measured with wind tunnel tests). For simplification, both WTS and lander are considered rigid. As detailed in Murdoch et al. (2016b), comparisons of rigid body assumptions with lander full finite element models including non-rigid parts do not exhibit significant differences in the produced stresses for the 0.01 to 1 Hz bandwidth.

The ground motion is generated by the feet and is felt by the seismometer. We have modeled the ground as an elastic half-space with properties of a Martian regolith. Due to the seismic velocities ($v_s = 150 \pm 17 \text{ m/s}$ and $v_p = 265 \pm 18 \text{ m/s}$) we assume that the propagation is instantaneous. No anelastic attenuation is taken into account at these frequencies

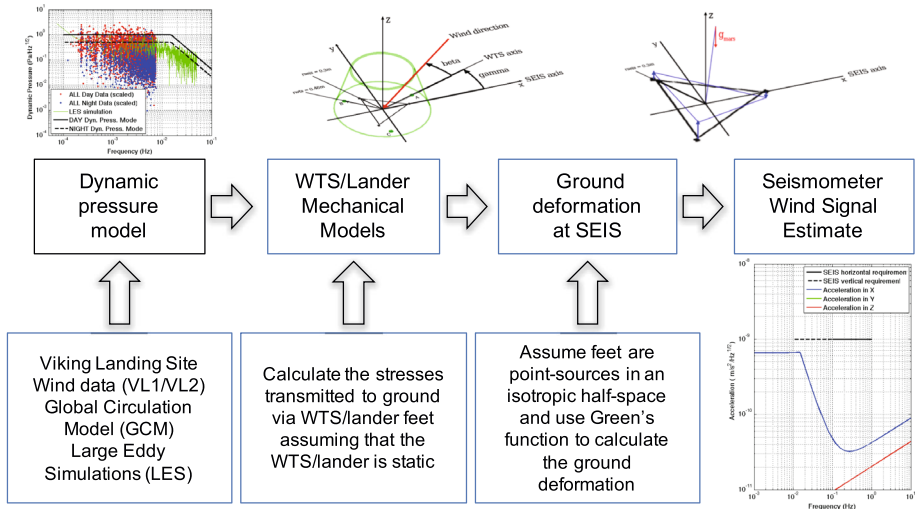


Fig. 21 Wind noise modeling summary

(only geometric spreading) and the results are, therefore, assumed to be the worst case (see Teanby et al. (2016)). See also Delage et al. (2017) for a more detailed model of the expected ground properties on Mars. The Greens-function modeling reveals two components to the acceleration: the direct motion of the ground, and the acceleration due to different SEIS feet vertical motions. The resulting effect causes the seismometer to tilt, measuring therefore the projection of the gravity field on its horizontal axes as a parasitic acceleration noise.

5.8.1 Noise Generated by the Lander

The noise generated by the lander vibrations under the effect of the wind is described in Fig. 22. As the noise value depends strongly on the location where the seismometer is deployed, we assumed that it is deployed at the baseline position (see Fig. 35). In Sect. 7 we will discuss the case where the seismometer is not deployed at its baseline position.

5.8.2 Noise Generated by the WTS and HP3

The noise generated by the WTS vibrations under the effect of the wind is described in Fig. 23. The noise level depends on the clocking of the WTS feet with respect to the seismometer feet. We make here the assumption that the clocking of the WTS puts the maximum distance from SEIS feet (this is a very likely configuration due to the rigidity of the cable that prevents the seismometer from turning during deployment). The computation for HP3 induced wind noise is similar, and turns out to be negligible unless both SEIS and HP3 are deployed very close to each other.

5.9 Pressure Tilt

The fluctuations of the pressure at the surface of Mars induce a response of the ground (due to the ground elasticity) that can be measured as a tilt by the InSight seismometer. Pressure

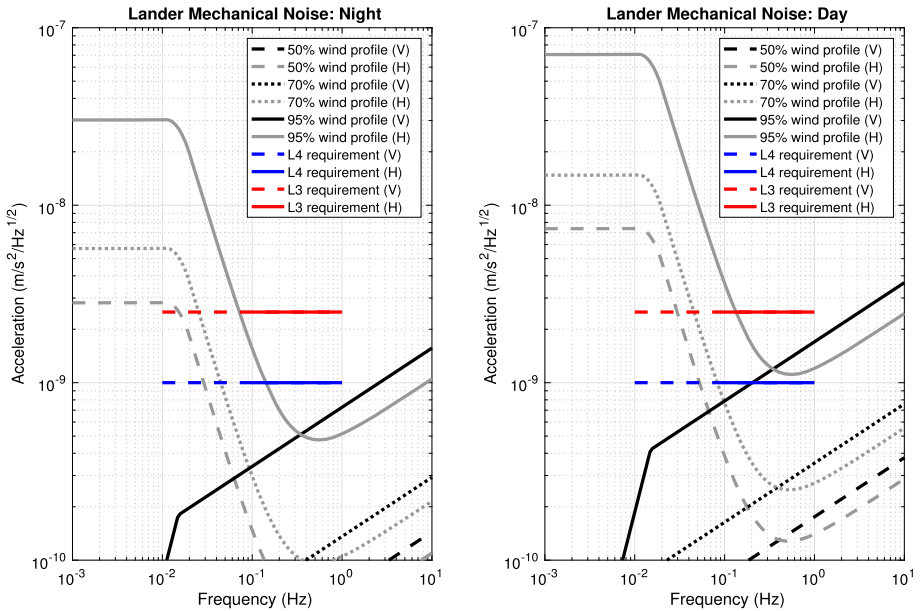


Fig. 22 Lander mechanical noise for various wind statistics—the (left) night time and (right) day time noise on the horizontal (light grey) and vertical (dark grey) axes due to the mechanical noise produced by the wind on the lander. Rather than show both the acceleration in x and y , the horizontal noise is the largest of the two contributors. The different lines show the predicted noise for the 50% wind profile, the 70% wind profile results and the 95% wind profile results. Also shown are the instrument level vertical and horizontal requirements (blue and dashed blue lines, respectively) and the system level vertical and horizontal requirements (solid red and dashed red, respectively). These simulations assume the baseline parameters including that the wind is coming exactly from a North-West direction

noise on Earth has been studied as it becomes a significant long-period noise source at 1–10 mHz—see Warburton and Goodkind (1977)) and several studies like Widmer (1995) propose that pressure signals may be decorrelated from the low frequency seismic signal.

The first estimate of tilt pressure noise on Mars has been made by Lognonné and Mosser (1993) who propose it as the main source of Martian seismic noise, in the absence of a global ocean. This estimate relies on the decomposition of the pressure field as a sinusoidal pressure wave, based on the theory developed by Sorrells’ model Sorrells et al. (1971), Sorrells (1971) in which both the wind and the pressure play a role. The general idea behind this modeling is that the ground displacement due to the pressure loading can be computed in the case where pressure fluctuations are plane waves propagating with a wind speed c .

The Sorrells’ et al. theory has been used in combination with the reference ground model and the elastic displacement for the reference model. (U , V , W) are not related to seismometer axes direction, but to the vertical direction (U), the direction of the pressure wave propagation (V) and the direction orthogonal to this propagation (W). For a simple half-space model, the resulting ground displacements (U , V , W) along the three orthogonal directions is given by:

$$U_{\text{Vertical}} = \frac{c_0 P_0 v_p^2}{2v_s^2 \rho (v_p^2 - v_s^2)} \frac{1}{\omega}$$

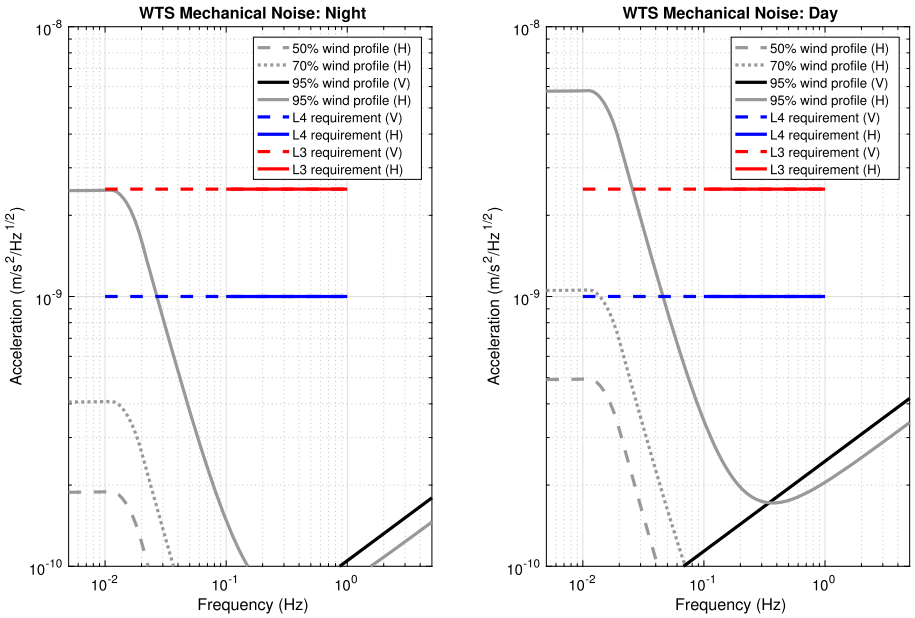


Fig. 23 WTS mechanical noise for various wind statistics—the (left) night time and (right) day time noise on the horizontal (light grey) and vertical (dark grey) axes due to the mechanical noise produced by the wind on the WTS. The different lines show the predicted noise for the 50% wind profile, the 70% wind profile results and the 95% wind profile results. Also shown are the instrument level vertical and horizontal requirements (solid black and dashed black lines, respectively) and the system level vertical and horizontal requirements (solid very light grey and dashed very light grey lines, respectively). HP3 noise is negligible with respect to WTS wind noise. These simulations assume the baseline parameters given in Appendix including that the wind is coming exactly from a North-West direction

$$V_{Horizontal} = -\frac{c_0 P_0}{2\rho(v_p^2 - v_s^2)} \frac{1}{\omega}$$

$$W_{Horizontal} = gU \frac{\omega}{c_0} = \frac{P_0 v_p^2}{2v_s^2 \rho(v_p^2 - v_s^2)} g$$

where c_0 is the wind amplitude, v_p is the p-wave velocity, v_s is the s-wave velocity, P_0 is the atmospheric pressure, ρ the bulk ground density, g is the gravitational acceleration, and ω the frequency of the considered signal. Note that U and V are both large for unconsolidated regolith (i.e., material with a low v_s).

The preliminary estimate of the Martian background noise made by Lognonné and Mosser (1993) was in the range of 10^{-8} to 10^{-9} $\text{m/s}^2/\sqrt{\text{Hz}}$. Elastic deformations are concentrated in the vertical direction for the body-wave frequency band (0.1–1 Hz), and horizontally for lower frequencies (<0.1 Hz, important for surface waves and normal modes). In order to make this contribution precise in our case, we have to evaluate the pressure field around the InSight landing site, then model the deformation of the ground at the seismometer location before deriving the induced noise in the seismic bandwidth. This section summarizes the approach we have followed, but the whole process is described in detail in the companion paper Murdoch et al. (2016a).

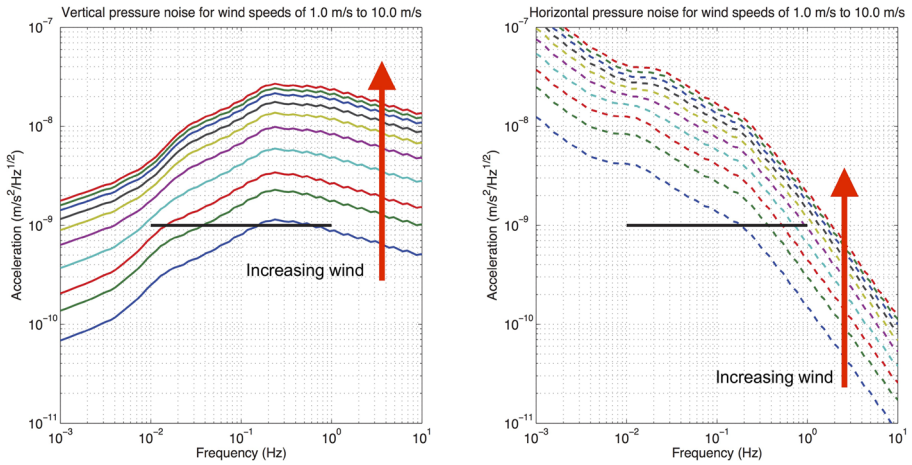


Fig. 24 Pressure noise computed with the Sorrells methods—sensitivity to Mean winds from 1 to 10 m/s—each colored line on the plot corresponds to a 1 m/s wind increase, with blue = 1 m/s and red (at the top) = 10 m/s. Pressure noise is very sensitive to mean winds. Solid lines in the figures show the instrument requirements level

5.9.1 Pressure Field Assumptions

The first step is to generate the pressure field around the InSight landing site in the correct time-frequency domain. In order to focus on the seismic bandwidth, we are interested in simulations of the pressure variations between 1 s and 100 s. This level of resolution of pressure field simulations is reached only by the Large Eddy Simulations (LES) that can resolve the turbulence-related phenomena at the interface between the Martian surface and the atmosphere, plus theoretical considerations for periods below 10 seconds. High resolution LES, as described in Spiga and Forget (2009) can use grids smaller than 50 m of resolution and can therefore simulate convective motions of the atmosphere as well as the large vortices and turbulent structures such as dust devils, which are expected to be the main source of turbulence related tilt noise in our bandwidth.

Once this pressure field is generated, we used first the Sorrells' theory—see Sorrells et al. (1971), Sorrells (1971), to compute a quasi-static ground displacement generated by the pressure loading of the computed field. This pressure field applies on the layered InSight reference ground model. The ground displacement is calculated for two wind speeds at the InSight landing site (4.5 m/s and 8 m/s) and then, as the vertical ground velocity is proportional to the mean wind, we assume a linear interpolation for other wind values (see Fig. 24).

In the Sorrells' theory the pressure fluctuations are plane waves propagating at the ambient wind speed. This is the model that has been used for computing the pressure tilt noise. In order to make a sanity check, we have also developed a quasi-static model using Green's function approach: a pressure field applies in a static way on a homogeneous half-plane. This simpler model gives very similar results, as described in Murdoch et al. (2016a). The advantage of this simpler model is that it can be considered as validated on Earth: Lorenz et al. (2015) has shown that the size and amplitude of seismic signal generated on a seismometer by a dust devil (which can be assimilated to a pressure point source) can be measured, and is consistent with the Greens' function approximation used.

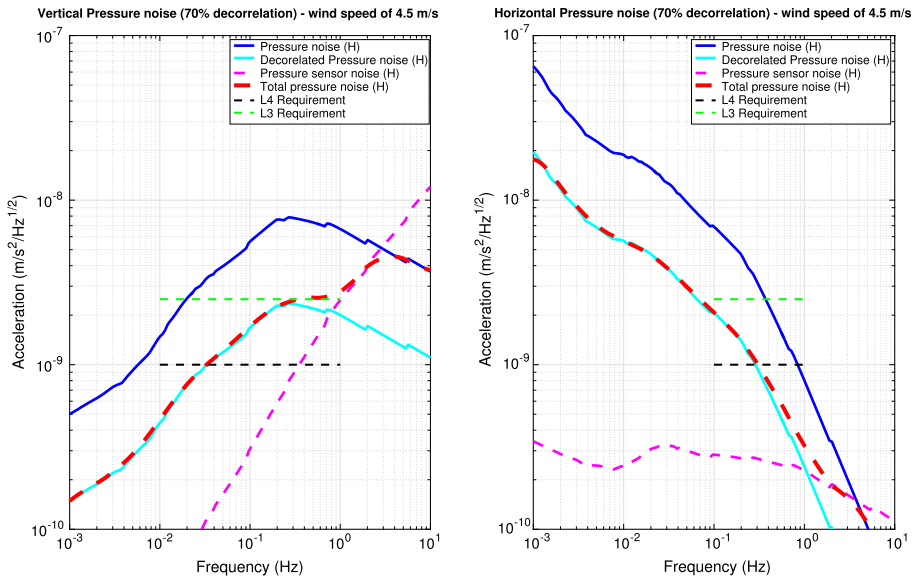


Fig. 25 Pressure noise contribution for a 4.5 m/s wind at the InSight landing site. This corresponds to the 1σ value of the noise. In *dark blue*, the pressure noise on vertical (*left*) and horizontal (*right*) axes. In *light blue*, the same noise with a decorrelation of 70% efficiency with a perfect barometer (no limiting self-noise). In *purple (dashed)*, the estimated self-noise of the InSight flight model micro-barometer. In *red*, the expected pressure noise after decorrelation (where possible) with the flight model micro-barometer. In *dashed black* and *green*, respectively, the expected performance requirements of the SEIS instrument (L4) and the SEIS system (L3). A discontinuity at around 1 Hz occurs when the microbarometer self-noise is of the same order of magnitude as the pressure noise

5.9.2 Pressure Field Decorrelation

Estimates of the pressure noise level on Mars without any decorrelation are about $10^{-8} \text{ m/s}_2/\sqrt{\text{Hz}}$ (see Fig. 24); far over the level allocated for the overall system noise (about $2.5 \times 10^{-9} \text{ m/s}_2/\sqrt{\text{Hz}}$). Similarly to the magnetic field impact, we foresee to reduce the atmospheric pressure seismic signals by making use of a microbarometer able to measure pressure fluctuations in the seismic bandwidth. This microbarometer is also part of the InSight APSS.

Contrary to the magnetic field noise, which only depends on the local value of the magnetic perturbation, the pressure tilt integrates the pressure perturbation over a large surface around the landing site. The correlation with a local measurement of the pressure variation can, therefore, be questioned. Murdoch et al. (2016a) demonstrate that the local tilt is well correlated with the local pressure measurement up to a distance of 1 to 4 km depending on the wind conditions (windier conditions induce a better correlation). By using the synthetic noise data obtained from the LES pressure field, we were able to demonstrate that our decorrelation approach is efficient, resulting in a reduction by a factor of ~ 5 observed in the horizontal tilt noise (in the wind direction) and the vertical noise. This technique can, therefore, be used to remove partially the pressure signal from the seismic data obtained on Mars during the InSight mission. Therefore, we have assumed decorrelation efficiency of 70% (see Fig. 25 for the resulting noise). Of course, local tilt effects may depend heavily on the local geology, but we expect the selected site subsurface structure to be very

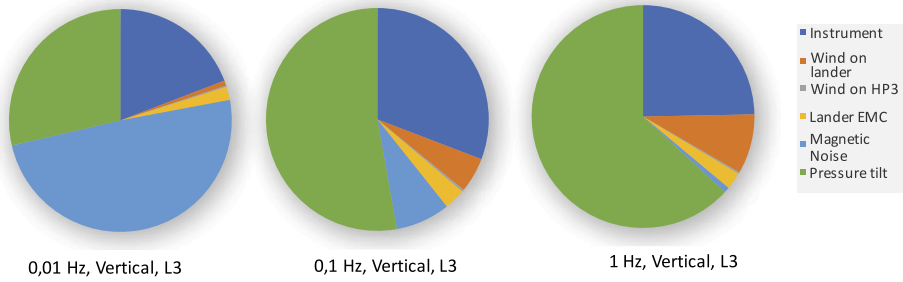


Fig. 26 Relative contributions of the noise model for the vertical noise relative to L3 requirements. From left to right, relative amplitudes of various noise for 0.01 Hz, 0.1 Hz, and 1 Hz. Note the major contribution of the pressure noise and magnetic noise with respect to instrument noise. *Green* is pressure tilt, *dark blue* instrument noise and *light blue* magnetic field noise

Table 4 Instrument noise sources table

Instrument noise	Description
VBB self noise	Instrument self-noise
VBB Thermal noise	Temperature impact on instrument
Thermoelastic tilt	Instrument distortion under thermal stress
Tether dilatation	Impact of tether thermal stresses on sensor assembly
Heaters	Thermoelastic resulting from switch on of heaters
Acquisition	E-box acquisition noise
Wind on WTS	Tilt on the instrument resulting from wind stresses

homogeneous—see Golombek et al. (2016). Nonetheless, the pressure contribution remains the dominant contributor to the overall noise model.

6 Noise Profiles

Once the major noise contributors are identified, we can make the summation of the various contributions. Let’s recall that the amplitude spectra of the time series describes the distribution of power into frequency components composing that signal. Error contributors deriving from the same environmental parameters such as the wind or the temperature are summed linearly (as they are likely in phase). Other noise sources are summed quadratically. Figures 26, 27, 28 and 30 to 33 present the sum of the major contributors for the instrument and system noise, respectively, relative to the system requirements. Note that, similarly as on Earth, the noise during the night time is significantly reduced. We then expect that a large fraction of the quake detection will be done during this quiet night time.

The typical values considered are 1σ (middle curves) but mean values of the noise and 3σ are also of interest.

6.1 Instrument Noise Summary

The instrument noise summary depicted in Table 4, 5, Figs. 26, 27 and 28 detail the various noise contribution sources at the instrument level. The resulting noise level is consistent with the requirements, close to $1.0 \times 10^{-9} \text{ m/s}^2/\sqrt{\text{Hz}}$ for the 1σ error model.

Fig. 27 Instrument L4 vertical (blue) and horizontal (red) noise estimates for *day* environmental conditions. Dashed black and black lines represent the instrument performance requirements. Performances are presented for mean (50%), nominal 1σ (70%) and worst case 3σ (95%) conditions—respectively in dashed, dot-dashed and plain lines

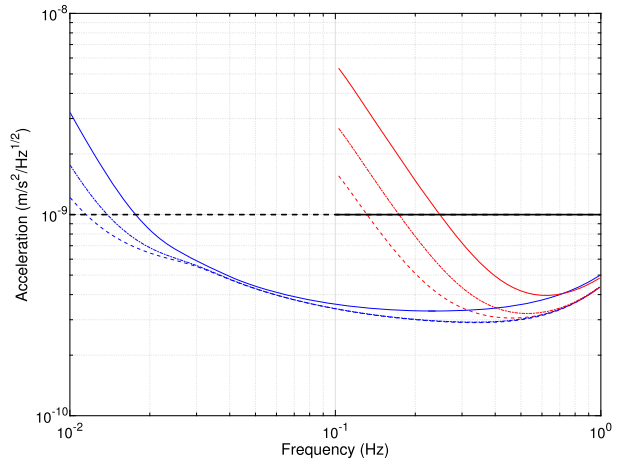


Fig. 28 Instrument L4 vertical (blue) and horizontal (red) noise estimates for *night* environmental conditions. Dashed black and black lines represent the instrument performance requirements. Performances are presented for mean (50%), nominal 1σ (70%) and worst case 3σ (95%) conditions—respectively in dashed, dot-dashed and plain lines

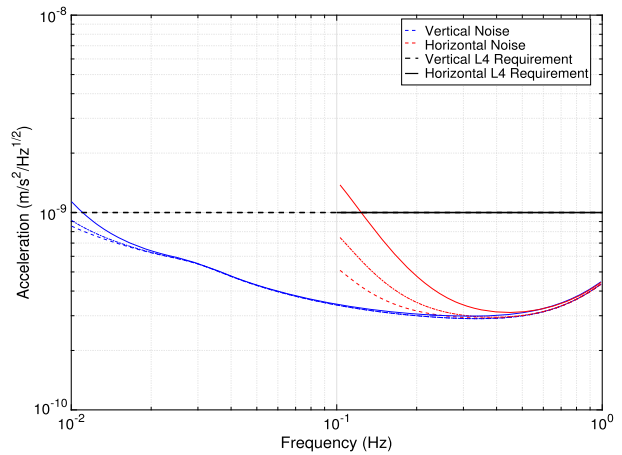


Table 5 System noise sources table

System noise	Description
Instrument noise	Complete instrument noise—see previous section
Wind on lander noise	Impact of the lander motion (tilt and acceleration)
Wind on HP3	Impact of the companion payload HP3
Lander EMC noise	Lander radiation
Magnetic noise	Magnetic field impact (decorrelated)
Pressure noise	Pressure noise (decorrelated)

6.2 System Noise Summary

The system noise summary (see e.g. Fig. 32) details the various noise contribution sources at the system level. As for the instrument, the noise increases significantly during the day

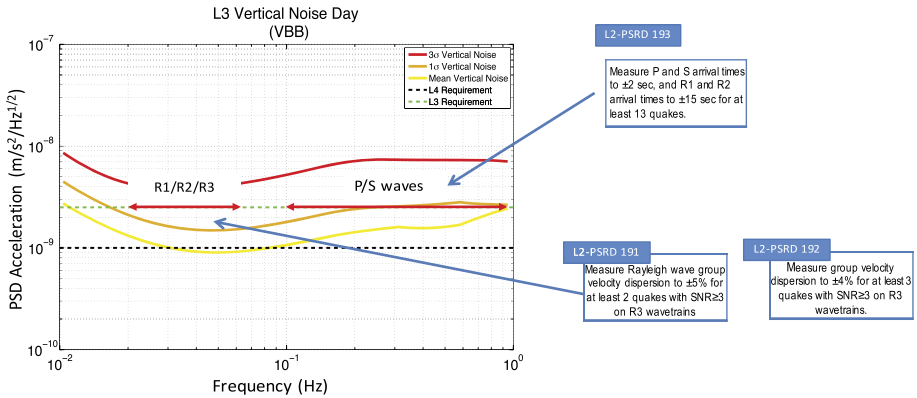


Fig. 29 Examples of sub-bandwidth of interest for the InSight Mission requirements. Even if the instrument/system requirements are not fully compliant, the noise value may still allow a sufficient SNR in a bandwidth of interest to fulfill the mission requirements

(mainly due to the pressure noise). We therefore expect quiet periods during the night, with an increased detection rate. The resulting noise level is consistent with the requirements, close to $2.5 \times 10^{-9} \text{ m/s}^2/\sqrt{\text{Hz}}$ for 1σ error model, even if it goes over this threshold at some frequencies. This is not a major issue.

As a matter of fact, it must be here noted that L3 and L4 requirements are a simplification of the ASD analyses that were used to derive the mission requirements. As a matter of fact, some mission requirements rely on P and S waves detection (mostly in the [0.1 1] Hz bandwidth) while other mission requirements rely on the detection of Rayleigh waves (mostly below 0.02 Hz). The signal to noise ratio applicable to these requirements is not computed on the overall requirement bandwidth, but on a smaller range, where the margins are better (see e.g. Fig. 29). In addition to this, compliance with respect to overall mission goals has to be evaluated on the full duration of the mission, including “day time”, “night time”, and “bad weather time” (approximately one third of the time each). A lower quake detection probability during bad weather is more than compensated by increased detection during the night. This general approach will be detailed in a forthcoming paper about the mission system approach.

7 Applications of the Noise Model

The SEIS noise model is a key element of InSight mission system design, and it has many applications, for both engineering and science aspects.

7.1 Instrument Performance Requirements Determination

The first application of the noise model was to help set up the various requirements for the instrument and the system. Given a first estimate of the various contributions, an estimate of the system performance is made, and compared with the detection capabilities. A typical example was described in Sect. 3: preliminary estimates of the total noise level were too high which led to the decision to implement a pressure sensor and a magnetometer to decrease the pressure tilt and magnetic noise contributions. The magnetometer and pressure sensor

Fig. 30 System L3 vertical a noise estimates for *day* (**bold green**) environmental conditions. *Dashed black lines* represent the instrument performance requirements. Performances are presented for mean (50%), nominal 1σ (70%) and worst case 3σ (95%) conditions in *dashed, dot-dashed and plain lines*, respectively

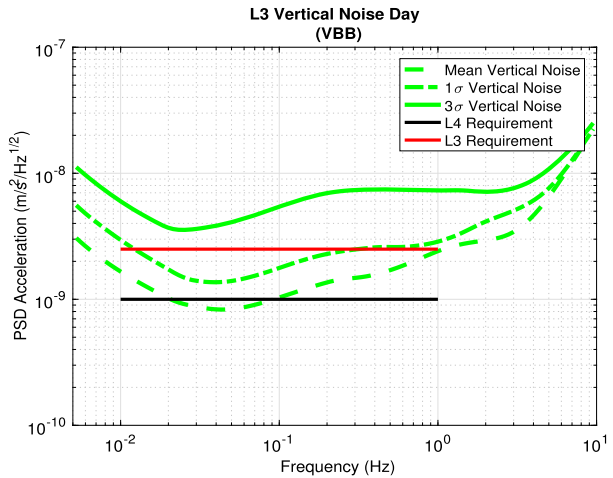
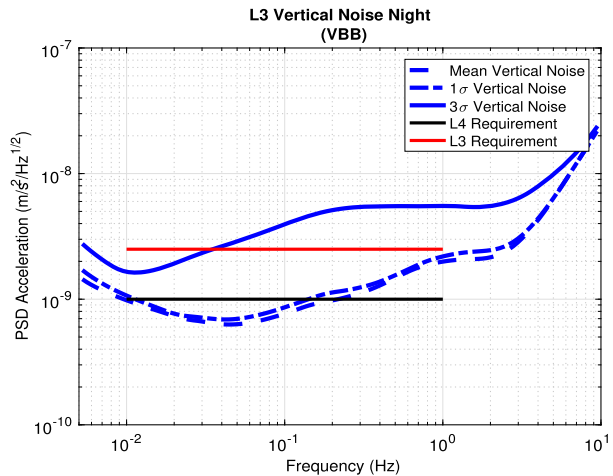


Fig. 31 System L3 vertical noise estimates for *night* (**bold blue**) environmental conditions. *Black and red lines* represent the performance requirements



performance requirements have also been derived from this model. In addition, later in the instrument development, the thermoelastic contribution of the tether has been found not compatible with the instrument budget; a design iteration has been made, introducing a tether shunt (which behaves like a terrestrial tether loop) to mitigate this issue.

7.2 Follow up of the System Performances

The noise model is also used to estimate the number of quakes that SEIS will detect as a function of the mission design and development (mission requirements are expressed in terms of the number of detections during the mission duration). The primary methods used to retrieve the internal structure are described in Panning et al. (2015, 2016) for the Internal structure and by Khan et al. (2016) and Böse et al. (2017) for the seismicity and source locations.

An instrument with a lower noise, or an instrument less sensitive to environmental perturbations, will detect more Marsquakes, which, in return, will allow a better resolution on the interior structure determination.

Fig. 32 System L3 horizontal noise estimates for *day* (*bold green*) environmental conditions. *Black and red lines* represent the performance requirements

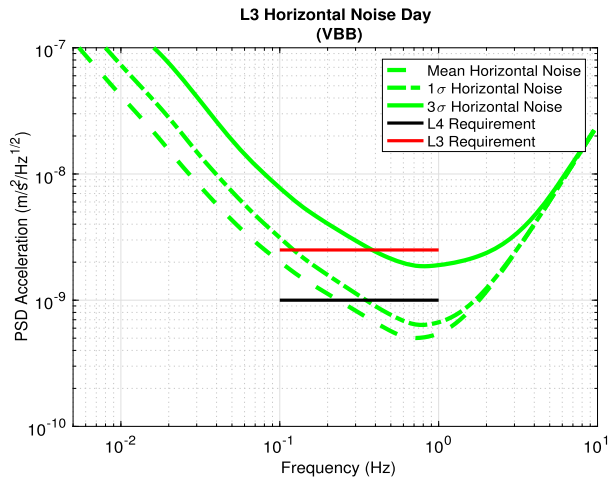
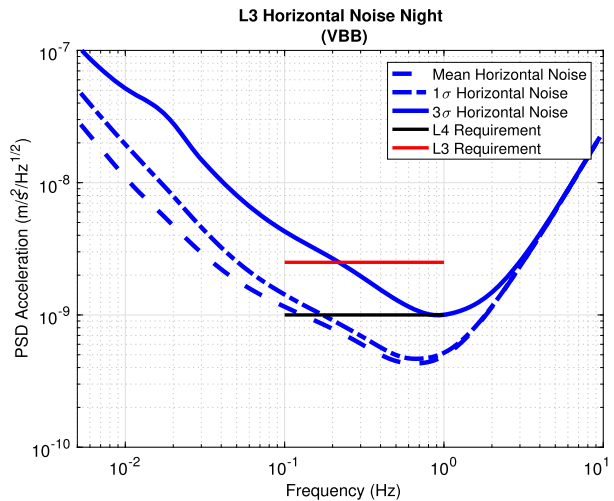


Fig. 33 System L3 horizontal noise estimates for *night* (*bold blue*) environmental conditions. *Black and red lines* represent the performance requirements

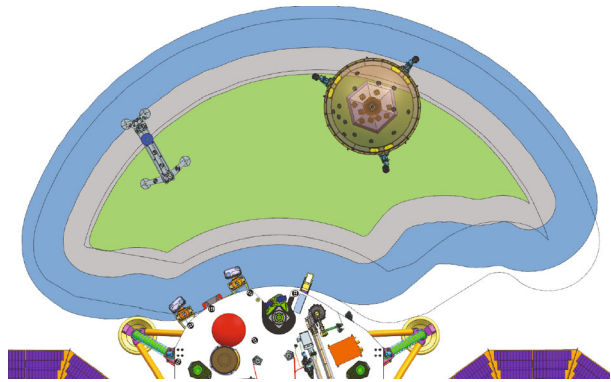


The first step is the estimation of quake probability as a function of the quake magnitude (smaller quakes should occur more frequently than bigger Marsquakes). This requires a Mars seismicity model, such as the one described in Lognonné and Johnson (2015).

Once the quake’s amplitude is known, interior structure model assumptions will help derive the amplitude of the quake waveform and the signal spectra at the various arrival times by the station and then its location Panning et al. (2015), Böse et al. (2017). Finally, comparison of the noise (self noise plus external noise) with this signal amplitude will give the detection capability. Of course, as the noise depends on the environmental conditions, the quake detection probability will be proportional to the environmental conditions, as described in Appendix B.

The total number of quakes detected depends on these various environmental conditions of the mission, but it also depends on the instrument and system availability: during SEIS re-centering, or during instrument or lander outage, the system is not available to record quakes. This has also been evaluated. Finally, given the small number of expected seismic events,

Fig. 34 Seismometer (*right*) and HP3 (*left*) in their nominal position in the deployment workspace—this derives from the mechanical capability of the lander arm—in *green* the possible positions for the seismometer, in *blue* the limit position for the WTS feet. The *gray* area is the limit for the HP3 deployment zone



a Poisson statistic has to be used to evaluate the probability of detections, as a function of time.

7.3 Use During Operations

One of the key contributors to the noise model is the mechanical noise of the lander transmitted through the ground to the seismometer (see Sect. 5.8.1). Of course, depending on the actual conditions on Mars, the mission may not be able to deploy the seismometer at its nominal location: the situation will be different, if the seismometer is deployed far from the lander, or if it has to be deployed next to a lander foot (the reference location is drawn Fig. 34).

As a direct consequence of the assumption that the ground behaves as an elastic medium, two major parameters influence the noise contribution of the lander: the distance to the lander feet, the mean slope on which the lander is located and the mean wind speed and direction. We have developed a tool described in Murdoch et al. (2016b) that will estimate the noise depending on the actual landing conditions and help us optimize the seismometer placement in the case where the baseline location is not available (this may occur, for example, if there are rocks over 3 cm, or if the slope is too steep). An example of output of this tool is shown Fig. 35 for the corner values of the seismic frequency band of interest.

7.4 Other Potential Applications and Follow-on Work

Many other applications can be made with the noise model: for example generating synthetic noise signals for internal structure inversion methods Panning et al. (2016), or trying to estimate the seismic “low noise model” of Mars. Ongoing studies—for example Pou et al. (2016) propose to extend this work to lower frequencies, in order to estimate the environment background for gravimetric applications of the seismometer, such as the Phobos tide measurements described by Van Hoolst et al. (2003).

8 Conclusion

This paper is a summary of the many studies that have been necessary to establish the complete seismic noise model for the InSight mission. It tries to use a balanced approach in the prediction of the expected mission performances on Mars, between the necessary caution required to design an instrument robust to any conditions that may happen, and a fair estimate

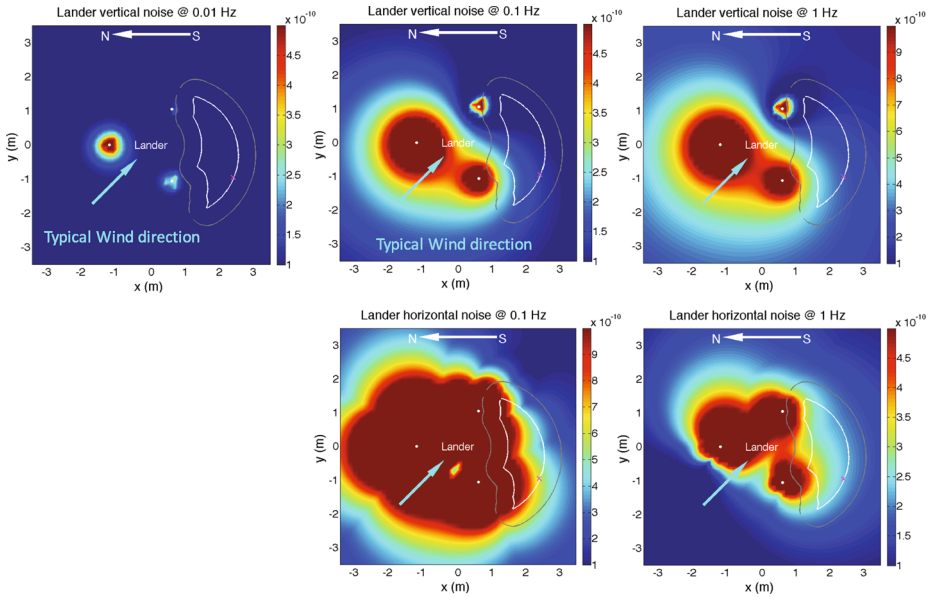


Fig. 35 Example of lander mechanical noise maps—for details on their generation see Murdoch et al. (2016b)—horizontal and vertical lander mechanical noise maps at 0.01 Hz, 0.1 Hz and 1 Hz. The units of the colour bars are $\text{ms}^{-2}/\sqrt{\text{Hz}}$. The colour code indicates the noise level with respect to the noise budget allocation for the lander mechanical noise, dark blue being far below the noise budget requirement and dark red is at, or above, the noise budget allocation. The three lander feet are indicated by the white circles, the possible SEIS and Wind and Thermal Shield deployment zones are indicated by the white and gray outlines, respectively. The SEIS baseline deployment location is indicated by the magenta cross. The wind direction is from the NW as indicated by the cyan arrow and the 70% day wind profile is used. Each image covers an area of 7 m by 7 m, centered on the geometric center of the lander

of the environment that SEIS will encounter on Mars. We have also chosen deliberately not to present the noise budgets table, of little scientific interest but of great use in the mission design and development.

At the time we are writing this paper, based on the analysis of the sizing system noise, the noise model predicts that the mission requirements based on the system noise in the seismic bandwidth [0.01 1] Hz will be fulfilled. Of course, this statement takes into account a few other assumptions on the system availability, and relies on the continuing good behavior of the seismometer and mission system hardware!

This paper is complemented by several papers, dealing with the details on the most dominant noise contributions such as pressure tilt noise or mechanical noise calculated in Murdoch et al. (2016a,b) and Kenda et al. (2016).

Appendix A: Minor Contributor Estimates

This section deals with minor contributors of the noise model.

A.1 Thermal Noise of the VBB Feedback Electronics

The VBB feedback electronics has its own sensitivity, and, as opposed to the VBB, is exposed only to the temperature profile inside the lander. There are requirements on the ther-

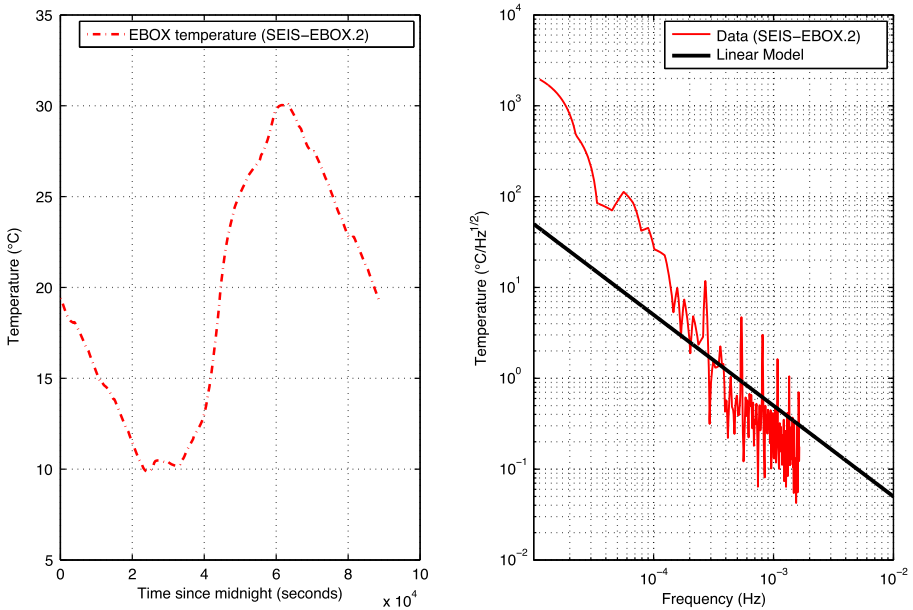
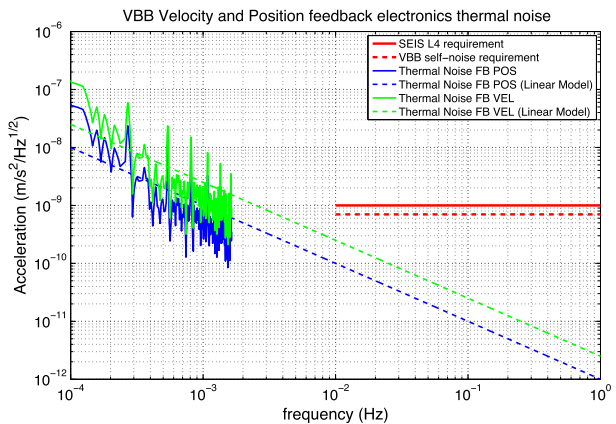


Fig. 36 *Left:* e-box temperature prediction (Courtesy Lockheed Martin). *Right:* temperature spectrum calculated from the data and a linear model used in the noise calculations. This is a worst-case example

Fig. 37 Electronics feedback temperature noise—this noise is included in the VBB self-noise. The large extrapolation of the linear model from the measured data is justified assuming that the EBOX thermal behaviour is similar to a low pass filter



mal sensitivity of the feedback (FB) electronics. The VBB POS output has a thermal sensitivity with respect to FB temperature less than $2 \times 10^{-9} \text{ m s}^{-2}/\text{K}$ below 0.01 Hz and $5 \times 10^{-8} \text{ m s}^{-2}/\text{K}$ over [0.01 0.1] Hz. The VBB VEL output shall have a thermal sensitivity with respect to FB temperature less than $5 \times 10^{-9} \text{ m s}^{-1}/\text{K}$ over [0.01 0.1] Hz and $2 \times 10^{-8} \text{ m s}^{-1}/\text{K}$ over [0.1 1] Hz. First the temperature profile within the E-box has been evaluated—see Fig. 36. Using the maximum thermal sensitivity, the thermal noise on the feedback electronics is calculated—see Fig. 37 and is found to be far below the L4 instrument noise requirement in both the horizontal and vertical directions.

A.2 Buoyancy

The buoyancy noise derives from the seismometer design; in order to keep the VBBs in high vacuum, they are enclosed in an evacuated sphere. As the local atmospheric density varies in time, the Archimedes tensor will act upon the sphere, resulting in a vertical force exerted on the regolith. The displacement of the seismometer equilibrium caused by such air density variations results in an acceleration noise on the vertical axis of the seismometers.

Using the local atmospheric density as a function of time, $\rho(t)$, from the Mars Climate Database (Lewis et al., 1999), it is possible to estimate the buoyancy noise on the sphere. Similarly to Sect. 5.9, we have assumed that the ground behaves as an elastic half-space, that the SEIS feet are rigid and cylindrical in shape and that the force is equally distributed between each of the three SEIS feet. We use Hertzian contact mechanics to calculate the vertical displacement $x(t)$ of each foot as a function of time.

$$x(t) = \frac{1}{3} \frac{F(t)}{2aE^*} = \frac{1}{3} \frac{mg - Vg\rho(t)}{2aE^*}$$

where V is the volume of the sphere, m is the mass of SEIS, g is the gravitational acceleration at the surface of Mars and a is the SEIS foot radius. E^* is a function of the Poisson's ratio and Young's modulus of the ground and of the LVL feet (see B).

The vertical acceleration due to the density fluctuations is computed. Finally, the spectrum for this acceleration is calculated. We then compare this to the buoyancy noise derived from the Mars Path Finder pressure measurements (see Sect. 5.3). We assume that the Martian atmosphere is adiabatic and the atmospheric density variations can, therefore, be described by the following equation:

$$\rho(t) = \rho_0 \left(\frac{P(t)}{P_0} \right)^k$$

where $\rho(t)$ is the atmospheric density as a function of time, ρ_0 is the mean atmospheric density, $P(t)$ is the atmospheric pressure as a function of time, P_0 is the mean atmospheric pressure and k is the adiabatic coefficient (1.28 for CO_2).

Again we calculate the vertical displacement (or indentation depth) of each foot, the vertical velocity and acceleration as a function of time. The buoyancy noise level in the range of [0.01–1] Hz is calculated to be $< 10^{-11} \text{ m/s}^2/\sqrt{\text{Hz}}$.

A.3 Noise Due to Dust Impact on the WTS

As SEIS is not buried but rather is deployed on the Martian surface, another potential noise resulting from the wind is the vibrations due to the aggregate mass of multiples, wind blown saltating sand particles on SEIS that may impact the Wind and Thermal Shield (WTS). The design of the WTS has been specifically tailored to minimize this impact: a weighted ≈ 10 cm high fabric skirt (reinforced by chainmail) provides both closure to inside the WTS and mechanical damping of dust effects on the WTS rigid structure.

Due to the geometry of the WTS (a cone section of ~ 30 cm diameter and ~ 30 cm height), we have assumed two kinds of effects:

- A direct impact coming from micron-size particles from the suspended dust in the wind flux (their quantity being estimated by opacity measurements): the acceleration on the WTS is proportional to the maximum wind spectrum. The effect can be scaled from the wind effect on the WTS, by estimating the mass load of the incoming wind, corrected by

the dust loading mass. This effect is negligible: as a matter of fact, the dust loading for an entire column of Mars atmosphere during a dust storm is estimated to about 4 g/cm^2 Martin (1995). Spread over the entire air column, this is to compare with the typical Mars atmospheric density (0.02 kg/m^3): it turns out that the contribution of dust loading is small with respect to the daily atmospheric density variations (0.0155 to 0.0220 kg/m^3).

– A secondary impact coming from “saltation particles” flux from saltation models Kok (2010): these heavier particles have mostly a ballistic trajectory and impact the WTS with a ≈ 45 deg angle. The saltation is initiated when the shear stress exerted by wind on the soil surface exceeds the fluid threshold Kok (2010), at which point surface particles are lifted Kok et al. (2012). These lifted particles undergo ballistic trajectories during which they are accelerated by wind drag. It is also worth pointing out that there is a low velocity zone at the leading surface of the WTS, and as the impact moves more to the side, the impact becomes more and more oblique.

However, in this last case, the saltation process is very unsteady. As underlined in Kok et al. (2012), as well as in Stout and Zobeck (1997), the saltation process depends on a threshold value of the shear stress near the surface Kok and Renno (2009). Therefore, this saltation effect is limited to a reduced period of time, when the wind velocity is over a threshold u^* . Following Kok (2010), the minimum wind shear speed (u^*) for saltation is about 0.5 m/s (for $100 \mu\text{m}$ grains). We can estimate the wind shear speed from the wind speed at one measurement location, $U_x(z)$, if we make an assumption on the surface roughness, z_o :

$$u^* = \kappa U_x(z) / \ln(z/z_o).$$

Here, we use the in-situ wind measurements from Phoenix, Viking Lander 1 and Viking Lander 2 to estimate the shear velocity statistics assuming a surface roughness (for the In-Sight landing site, $z_o \approx 3 \text{ cm}$). The influence of the surface roughness on the shear wind speed statistics is also investigated (shear wind speed increases with surface roughness; see Fig. 38). For most of the measured wind speeds, the shear wind speed stays below the threshold.

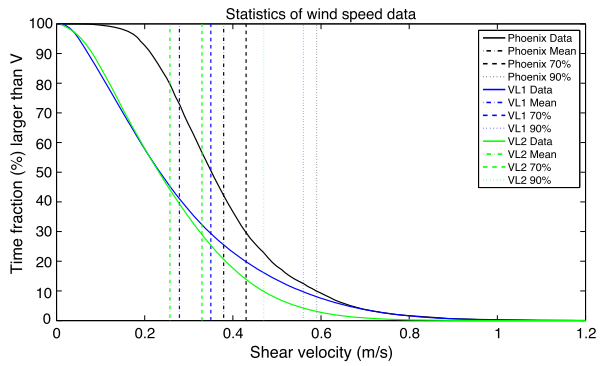
The shear wind variability has also been estimated, as a function of the local time on the basis of the in-situ wind measurements (Fig. 38). For most of the time, even small particles ($100 \mu\text{m}$ grains) are not uplifted (see Fig. 39). Though there are instances in which it may be significant, we can conclude that saltation noise will be triggered by very specific wind conditions: it is expected to occur during “bad weather” periods, excluded from our typical 1σ statistics.

A.4 Electric field impact

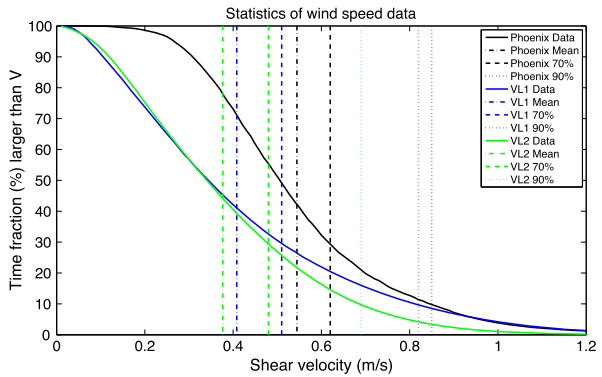
Even if no electric field has been recorded yet on Mars (ExoMars 2016 will carry an electric field measurement experiment described in Déprez et al. 2015), there are several possible physical phenomena that could generate one, ranging from electrostatic charging to possible thunderstorms—see Melnik and Parrot (1998). Among these processes, the saltation process and the transport of wind-blown sand, as well as dust storms and dust devils can produce local electric fields at the surface of Mars, see Kok and Renno (2008). Even if SEIS’ sensitivity to external electric fields is minimized by the grounding scheme of the instrument, the tether is sensitive to the variations of the electric field and therefore SEIS measurement could in principle be influenced by such phenomena.

Similarly to the temperature and magnetic field noise determination, the electric field noise is estimated in several steps. First, an experimental tether sensitivity to the electric

Fig. 38 Combined shear velocity statistics: even in the surface roughness worst case (5 cm), the wind shear velocity is below 1 m/s 90% of the time

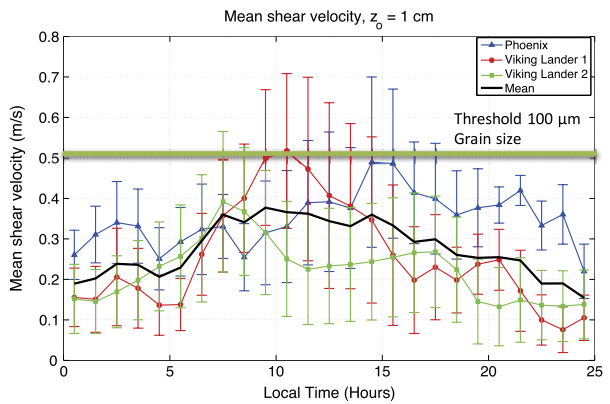


(a) Combined shear velocity statistics for 1 cm surface roughness (InSight landing site)



(b) Combined shear velocity statistics for 5 cm surface roughness

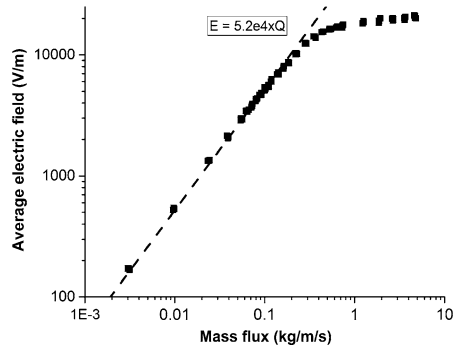
Fig. 39 Combined mean shear velocity vs local time, compared to 100 μm wind speed saltation threshold



field is estimated. Next, an estimate is made of the electric fields that are likely to be found at the surface of Mars. Finally, these are combined to determine the electric field noise on SEIS.

The E-field noise has been modeled as an additional voltage noise that comes into the VBB feedback loop at the integrator level. From the VBB feedback loop design, the transfer function between the VBB outputs and a noise added at integrator level is well known (it is

Fig. 40 Electric field generated as a function of the saltation mass flux (private communication, Kok, 2015)



an acceleration divided by Volt quantity depending on the frequency). Tests were performed in order to determine the worst case susceptibility of one meter of tether to the E-field (Tether E-field sensitivity CNES report, Schandler et al., 2015). Assuming a tether with a 70 cm vertical component and 3 m flat/horizontal component (similar to the flight model) the sensitivity is extrapolated to be $4 \mu\text{V}/\text{kV}/\text{m}$.

If grain transport occurs, there is an electric field that develops at the surface of Mars. The electric field generated as a function of the saltation mass flux is presented in Fig. 40. However, if there is no grain transport, there is no electric field and thus no electric field noise on SEIS. From the previous section, which analyzes the conditions for saltation initiation on InSight landing site, we can conclude that perturbation by in-situ electric fields will also be triggered by very specific wind conditions (storm, dust devils, ...). Such conditions are already included in the fraction of the time (“bad weather”) where the performance is already strongly degraded by environmental conditions.

Appendix B: Summary of Environment Assumptions

This appendix is a summary of the environment assumptions.

(See Fig. 41 for a summary of the chosen approach.)

B.5 Temperature Assumptions

Martian temperature spectra used (see Figs. 42, 43) are derived from Mars PathFinder and Viking data. Two types of datasets are derived from these data. A first “short term” dataset is used for the noise analysis. As a matter of fact, if we are interested in the seismic bandwidth (and its daily variation) for the noise model, the peak-to-peak temperature excursion is also important, in order to assess potential saturation issues on the VBB sensors. PathFinder measurements have been recorded at higher frequency, and Viking measurements have a lower frequency, but are ranging over a longer time span, including seasonal variations.

For the “short period” spectrum, we are mostly using Mars Path Finder data from a period of approximately 10 sols (sols 18–27 of the mission; data obtained from the Planetary Data Server). These data are chosen as they span several sols and have a sampling rate high enough to be compatible with our bandwidth requirements. Temperature data are first corrected for both the seasonal climate variations and the daily harmonics, leaving the residual temperature variations, from which the temperature residuals that the spectra are calculated. The linear models then correspond approximately to the mean, 1σ and 3σ spline fits of the

Environment factor	Model used for SEIS design (3σ / 1σ / mean)	Reason for choice
Temperature spectra	3σ	Temperature variations are critical for many parts of the design such as the SEIS thermal sensitivity. The 3σ linear model is used to ensure that SEIS can always meet the performance criteria.
Wind speed squared spectra	3σ	As the wind speed spectra at high frequency is based only on theoretical arguments (no in-situ data) the 3σ linear model has been used.
Wind speed	1σ	The wind speed is expected to be a perturbation with high seasonal variability (dust storm season). It is more appropriate to design the system on a 1σ value than on dust storm season assumptions.
Ground model seismic velocities	3σ	The ground stiffness calculated with the 3σ seismic velocities is consistent with the axial compression tests.
Magnetic field spectra	1σ	These were the only data available at the time.
Gravity	Mean	There are only very small variations in the gravity within the InSight landing site

Fig. 41 Summary of the environment assumptions

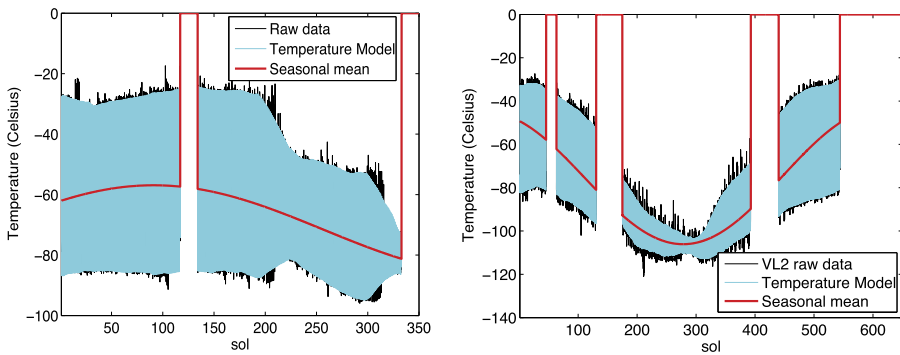


Fig. 42 Viking Lander temperature model and seasonal means. (a) The Viking Lander 1 and (b) the Viking Lander 2 temperature data with bad data removed (*black*), the temperature model (*cyan*) and the seasonal mean (*red line*)

spectra of the residuals at low frequencies. They are then separated into a “day” and “night” spectra based on the local hour of the data used to generate the spectrum. A “day” spectrum is entirely within the day period, a “night” spectrum is entirely within the night period. The daytime period was chosen arbitrarily to be from 6 am to 6 pm (night is from 6 pm to 6 am).

At longer periods Viking data are used. First, places where the Viking Lander sampling was interrupted (i.e., the time between two samples is much larger than the normal time between samples) and missing temperature data points are thus identified in the raw Viking Lander data. Periods when either the sampling was interrupted for too long (more than 40 sols) or too many consecutive data points were missing in the raw data for the data to be meaningful were removed the data set. The remaining bad temperature data points (indicated by a temperature of -273.15 C) were replaced with the mean temperature over the entire data set. It is necessary to remove the daily and seasonal temperature variations in order to

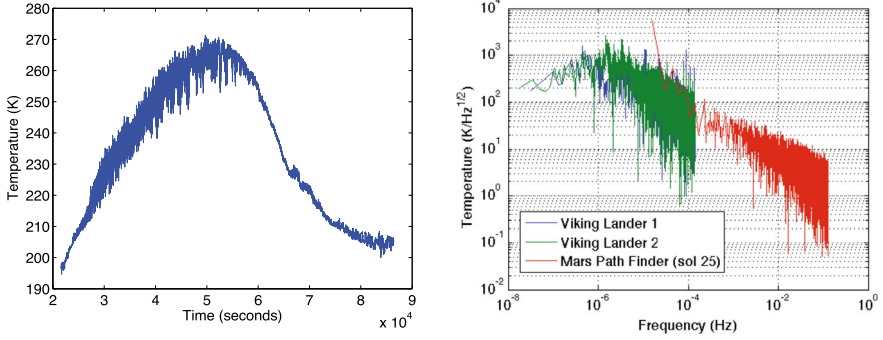


Fig. 43 Mars Pathfinder temperature data and spectrum. (a) Mars Pathfinder atmospheric temperature at the height of the bottom-mast thermocouple (sequence 1030 from sol 25) as a function of time. (b) Spectra of the VL1 (blue), VL2 (green) and MPF temperature data (red)

Fig. 44 Linear temperature model amplitudes

Model	Day	Night
3σ linear temperature model amplitude (K)	10	2.5
1σ linear temperature model amplitude (K)	10/2	2.5/2
mean linear temperature model amplitude (K)	10/3.5	2.5/3.5

remove the harmonics in the final temperature spectrum. To do this a temperature model is derived taking into account the seasonal climate variations and the daily harmonics.

In order to simplify the analysis, linear temperature models are derived from the data (Fig. 45). The temperature models are defined as a function of frequency (f) with amplitude (A) and cut-off frequency f_{cut} of ~ 0.1 Hz i.e.:

$$f < f_{cut} : T_m(f) = A \sqrt{\frac{f_{cut}}{f}}$$

and

$$f \geq f_{cut} : T_m(f) = A \frac{f_{cut}}{f}$$

For both the day and night spectra, we define a $\sim 1\sigma$ model, a $\sim 3\sigma$ model and a mean model. The amplitudes of these linear models are determined by calculating a mean spectrum (using a spline fit) and the standard deviation (1σ) of the mean spectrum. As the data cannot be fit perfectly by the linear model, we assume conservative amplitudes (particularly during the day time and within the SEIS bandwidth). The amplitudes of the linear temperature models are given in the Table 44:

B.6 Summary of Ground Properties

Two types of laboratory tests have measured regolith properties using a Martian regolith simulant: seismic velocity tests and axial response tests. In the complete InSight seismic noise model presented here, the seismic velocity measurements are extrapolated to the Martian environment. The three ground stiffness predicted for under the three SEIS feet on Mars (Fig. 46) are consistent with results from Delage et al. (2017).

Fig. 45 Temperature statistics derived from Mars Pathfinder data. Day related data (in red) are significantly higher than night data (in blue). Simplified spectra corresponding to mean, 1σ and 3σ fit are presented, in green for night time and yellow for day time, respectively in dashed, dot-dashed and plain lines. The data are consistent with long-period data from the Viking missions

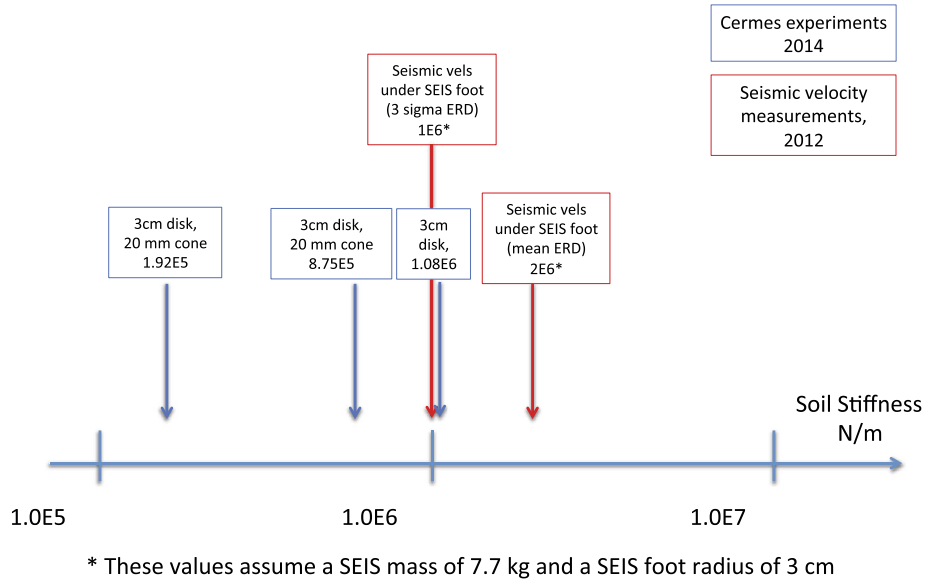
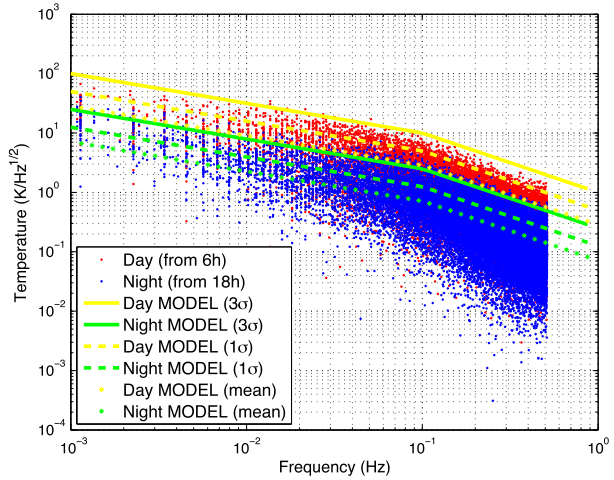
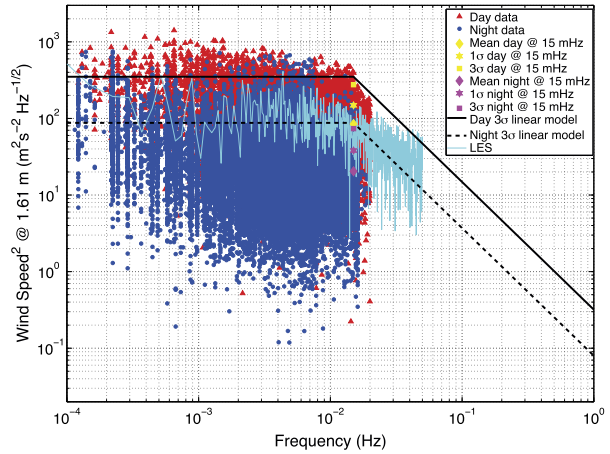


Fig. 46 Soil stiffness summary of measurements. CERMES experiments refer to Delage et al. (2017)

B.7 Wind Assumptions

Martian wind speed squared spectra are derived from Phoenix data, VL1 and VL2 data (Figs. 47, 48). The form of the linear models comes from the data at low frequencies, and from theoretical arguments at high frequencies. The amplitudes of the flat section of the linear models correspond approximately to the mean, 1σ and 3σ amplitudes of the wind speed squared spectra at 15 mHz (the estimated cut-off frequency between two regimes). When determining the wind speed at different heights, the complete InSight seismic noise model presented here assumes that the surface roughness length on Mars is 3 cm. See Murdoch et al. (2016b) for more details of the wind analyses.

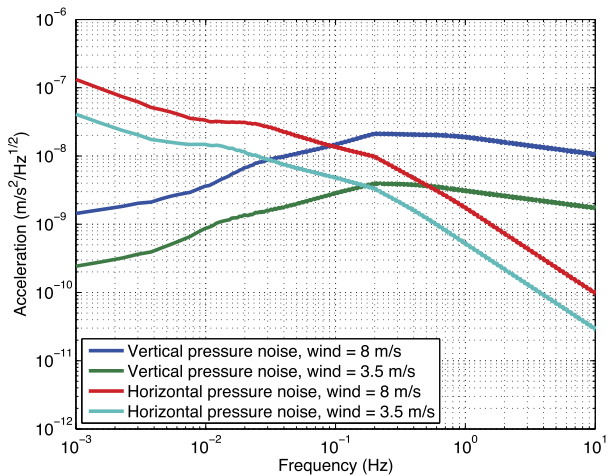
Fig. 47 Wind statistics used in the noise model



	Day 99-percentile ⁽¹⁾ wind speed at 1.6 m (m/s)	Day 70-percentile ⁽¹⁾ wind speed at 1.6 m (m/s)	Day 50-percentile ⁽¹⁾ wind speed at 1.6 m (m/s)	Night 99-percentile ⁽¹⁾ wind speed at 1.6 m (m/s)	Night 70-percentile ⁽¹⁾ wind speed at 1.6 m (m/s)	Night 50-percentile ⁽¹⁾ wind speed at 1.6 m (m/s)
VL1	11.4	5.6	4.45	5.6	2.7	2.1
VL2	9.1	4.5	3.55	7.2	2.9	2.44
Phoenix	11.30	5.8	4.98	8.10	5.0	4.34

Fig. 48 In order to be as close as possible from the ground truth, we have chosen to use Viking Lander 2 wind statistics in the ISAE SEIS noise model

Fig. 49 Reference pressure tilt for two typical wind speed assumptions 3.5 m/s and 8 m/s—data from Lognonné et al. (2016)—LES simulations at landing site from Spiga et al. (2012), private communication



B.8 Pressure Tilt Assumptions

The pressure noise is a ground tilt induced by pressure fluctuations caused by the wind. A pressure and wind field has been generated around the landing site thanks to a LES simulation as described in Spiga and Forget (2009). The resulting pressure noise tilt (vertical and horizontal) is estimated at two wind speeds by Sorrels method (see Fig. 49). An extensive

Fig. 50 Magnetic field assumptions—data from Johnson et al., (2016), private communication

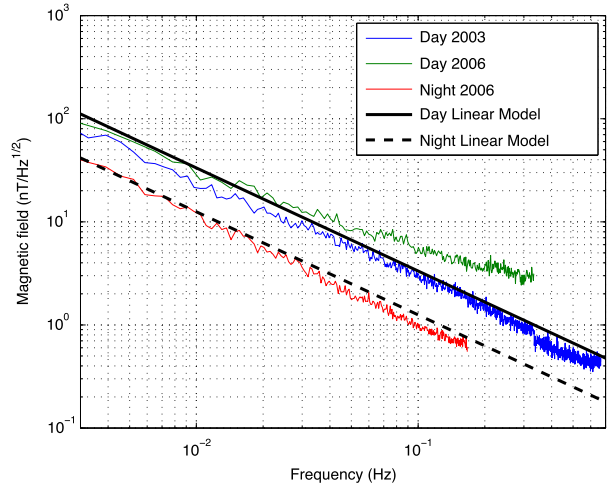
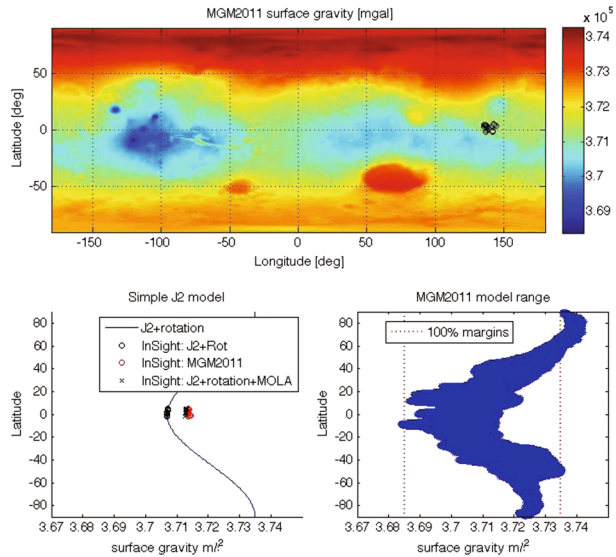


Fig. 51 Gravity field assumptions—data from Hirt et al. (2012)



description of the methods is provided in Murdoch et al. (2016a) and Kenda et al. (2016). Our noise model extrapolates from these values for intermediate wind speeds.

B.9 Magnetic Field assumptions

No magnetic data have ever been recorded at the surface of Mars. Therefore, the magnetic field at the surface (see Fig. 50) is estimated using in-orbit measurements (e.g. Langlais et al. 2004) extrapolated with new data (Johnson et al., 2016, private communication). Several MGS tracks from 2003 and 2006 have been used to retrieve the crustal magnetic field variations. These measurements have been corrected for spatial variations (motion of the satellite) and show only external field variations. The linear model is based on the 70% ($\sim 1\sigma$) spectrum.

Table 6 InSight seismic noise model key hardware parameter assumptions—current best estimates at the time of publication

Parameter	Units	Value
VBB magnetic sensitivity (Vertical)	$\text{m/s}^2/\text{T}$	$3.8\text{e-}10$
VBB magnetic sensitivity (Horizontal)	$\text{m/s}^2/\text{T}$	$1.9\text{e-}10$
SP magnetic sensitivity	$\text{m/s}^2/\text{T}$	$5.0\text{e-}10$
VBB thermal sensitivity (vertical and horizontal)	$\text{m/s}^2/\text{K}$	$2\text{e-}5$
SP thermal sensitivity (vertical)	$\text{m/s}^2/\text{K}$	$2.5\text{e-}5$
SP thermal sensitivity (horizontal)	$\text{m/s}^2/\text{K}$	$3.5\text{e-}5$
Sphere/LVL thermoelastic tilt sensitivity	deg/K	$5.4\text{e-}5$
Tether thermoelastic tilt sensitivity (for a ground stiffness of $1\text{e}6 \text{ N/m}$)	rad/K	$1\text{e-}11$
Tether electrical sensitivity	V/kV/m	$4\text{e-}6$
WTS thermal time constant	minutes	432
Sphere thermal time constant	minutes	180
SP-Box thermal time constant	minutes	7.6
Tether thermal time constant	minutes	24

B.10 Gravity Assumptions

There are only small variations in the gravity field on the surface of Mars in the InSight landing site. A value of 3.71 m/s^2 is always used in the ISAE SEIS noise model (see Fig. 51). The model used is described in Hirt et al. (2012).

Appendix C: Other Noise Model Parameters of Interest

In Table 6 are described the key hardware parameters used in the noise model. These are the best current estimates at the time of publication. For more details about the mechanical noise (lander, WTS, HP3) parameters, the reader is referred to Murdoch et al. (2016b).

Acknowledgements This work has been supported by CNES and by ISAE, including funding for post-doctoral support provided to N. Murdoch. ATA engineering (USA) performed the tether thermoelastic studies, and Mecano ID did the SEIS thermoelastic studies. Thanks for Jane Hurley (Oxford U) for her contributions. Thanks to Nicolas Verdier (CNES) for his support on the performance tests, and Taichi Kawamura for the VBB magnetic sensitivity analyses. Thanks to the VBB project manager (S. de Raucourt) and VBB instrument team for providing the VBB noise model (T. Nebut, O. Robert), VBB Temperature performances (S. Tillier, P.A. Dandonneau), and validating these models (M. Parise, T. Gabsi, M. Drilleau). The author wishes to thank J. Gagnepain-Beyneix, which was involved from the beginning in the noise model.

References

- D.L. Anderson, W. Miller, G. Latham, Y. Nakamura, M. Toksöz, A. Dainty, F. Duennebieber, A.R. Lazarewicz, R. Kovach, T. Knight, *Seismology on Mars*. *J. Geophys. Res.* **82**(28), 4524–4546 (1977)
- E. Arias, B. Beaudoin, R. Woodward, K. Anderson, A. Reusch, Relative noise level comparison of portable broadband seismometer installation techniques used by PASSCAL and flexible array, in *AGU Fall Meeting Abstracts*, vol. 1 (2014), p. 4474

- M. Böse, J.F. Clinton, S. Ceylan, F. Euchner, M. van Driel, A. Khan, D. Giardini, P. Lognonné, W.B. Banerdt, A probabilistic framework for single-station location of seismicity on Earth and Mars. *Phys. Earth Planet. Inter.* **262**, 48–65 (2017). doi:[10.1016/j.pepi.2016.11.003](https://doi.org/10.1016/j.pepi.2016.11.003)
- S. De Raucourt, T. Gabsi, N. Tanguy, D. Mimoun, P. Lognonne, J. Gagnepain-Beyneix, W. Banerdt, S. Tillier, K. Hurst, The VBB SEIS experiment of InSight, in *39th COSPAR Scientific Assembly*. COSPAR Meeting, vol. 39 (2012), p. 429
- P. Delage, F. Karakostas, A. Dhemaied, M. Belmokhtar, P. Lognonné, M. Golombek, E. De Laure, K. Hurst, J.-C. Dupla, S. Keddar et al., An investigation of the mechanical properties of some martian regolith simulants with respect to the surface properties at the insight mission landing site. *Space Sci. Rev.*, 1–23 (2017)
- G. Déprez, F. Montmessin, O. Witasse, L. Lapauw, F. Vivat, S. Abbaki, P. Granier, D. Moirin, R. Trautner, R. Hassen-Khodja et al., Micro-ares, an electric field sensor for ExoMars 2016, in *European Planetary Science Congress 2015*, vol. 10 (2015), EPSC2015-508
- T. Forbinger, Recommendations for seismometer deployment and shielding. in *New Manual of Seismological Observatory Practice*, vol. 2 (2012), pp. 1–10
- T. Forbriger, R. Widmer-Schmidrig, E. Wielandt, M. Hayman, N. Ackerley, Magnetic field background variations can limit the resolution of seismic broad-band sensors. *Geophys. J. Int.* **183**(1), 303–312 (2010)
- N.R. Goins, A.R. Lazarewicz, Martian seismicity. *Geophys. Res. Lett.* **6**, 368–370 (1979). doi:[10.1029/GL006i005p00368](https://doi.org/10.1029/GL006i005p00368)
- M. Golombek, D. Kipp, N. Warner, I.J. Daubar, R. Fergason, R.L. Kirk, R. Beyer, A. Huertas, S. Piqueux, N.E. Putzig, B.A. Campbell, G.A. Morgan, C. Charalambous, W.T. Pike, K. Gwinner, F. Calef, D. Kass, M. Mischna, J. Ashley, C. Bloom, N. Wigton, T. Hare, C. Schwartz, H. Gengl, L. Redmond, M. Trautman, J. Sweeney, C. Grima, I.B. Smith, E. Sklyanskiy, M. Lisano, J. Benardini, S. Smrekar, P. Lognonné, W.B. Banerdt, Selection of the insight landing site. *Space Sci. Rev.* (2016). doi:[10.1007/s11214-016-0321-9](https://doi.org/10.1007/s11214-016-0321-9)
- C. Hirt, S. Claessens, M. Kuhn, W. Featherstone, Kilometer-resolution gravity field of Mars: Mgm2011. *Planet. Space Sci.* **67**(1), 147–154 (2012)
- B. Kenda, P. Lognonné, A. Spiga, T. Kawamura, S. Kedar, W. Banerdt, R. Lorenz, D. Banfield, M. Golombek, Modeling of ground deformation and shallow surface waves generated by martian dust devils and perspectives for near-surface structure inversion. *Space Sci. Rev.* (2016)
- A. Khan, M. van Driel, M. Böse, D. Giardini, S. Ceylan, J. Yan, J. Clinton, F. Euchner, P. Lognonné, N. Murdoch et al., Single-station and single-event marsquake location and inversion for structure using synthetic martian waveforms. *Phys. Earth Planet. Inter.* **258**, 28–42 (2016)
- J.F. Kok, N.O. Renno, Electrostatics in wind-blown sand. *Phys. Rev. Lett.* **100**(1), 014501 (2008). doi:[10.1103/PhysRevLett.100.014501](https://doi.org/10.1103/PhysRevLett.100.014501)
- J.F. Kok, N.O. Renno, Electrification of wind-blown sand on Mars and its implications for atmospheric chemistry. *Geophys. Res. Lett.* **36**, 05202 (2009). doi:[10.1029/2008GL036691](https://doi.org/10.1029/2008GL036691)
- J.F. Kok, An improved parameterization of wind-blown sand flux on mars that includes the effect of hysteresis. *Geophys. Res. Lett.* **37**(12) (2010)
- J.F. Kok, E.J. Parteli, T.I. Michaels, D.B. Karam, The physics of wind-blown sand and dust. *Rep. Prog. Phys.* **75**(10), 106901 (2012)
- C. Kroner, BFO and Moxa: two observatories for seismological broadband observations, 2016. http://www.orceus-eu.org/website_until_17aug2016/organization/Organization/Newsletter/vol2no3/jena.html
- B. Langlais, M. Purucker, M. Manda, Crustal magnetic field of Mars. *J. Geophys. Res., Planets* **109**(E2) (2004)
- V. Linkin, A.-M. Harri, A. Lipatov, K. Belostotskaja, B. Derbunovich, A. Ekonomov, L. Khloustova, R. Kremnev, V. Makarov, B. Martinov, D. Nenarokov, M. Prostov, A. Pustovalov, G. Shustko, I. Järvinen, H. Kivilinna, S. Korpela, K. Kumpulainen, A. Lehto, R. Pellinen, R. Pirjola, P. Riihelä, A. Salmiinen, W. Schmidt, T. Siili, J. Blamont, T. Carpentier, A. Debus, C.T. Hua, J.-F. Karczewski, H. Laplace, P. Levacher, P. Lognonné, C. Malique, M. Menvielle, G. Mouli, J.-P. Pommereau, K. Quoth, J. Runavot, D. Vienne, F. Grunthaner, F. Kuhnke, G. Musmann, R. Rieder, H. Wänke, T. Economou, M. Herring, A. Lane, C.P. McKay, A sophisticated lander for scientific exploration of Mars: scientific objectives and implementation of the Mars-96 Small Station. *Planet. Space Sci.* **46**, 717–737 (1998). doi:[10.1016/S0032-0633\(98\)00008-7](https://doi.org/10.1016/S0032-0633(98)00008-7)
- P. Lognonné, C. Johnson, Planetary seismology. *Planets and Moons* (2015). doi:[10.1016/B978-0-444-53802-4.00167-6](https://doi.org/10.1016/B978-0-444-53802-4.00167-6)
- P. Lognonné, J.G. Beyneix, W.B. Banerdt, S. Cacho, J.F. Karczewski, M. Morand, Ultra broad band seismology on InterMarsNet. *Plan. Space Sci.* **44**, 1237 (1996). doi:[10.1016/S0032-0633\(96\)00083-9](https://doi.org/10.1016/S0032-0633(96)00083-9)
- P. Lognonné, D. Giardini, B. Banerdt, J. Gagnepain-Beyneix, A. Mocquet, T. Spohn, J.F. Karczewski, P. Schibler, S. Cacho, W.T. Pike, C. Cavoit, A. Desautez, M. Favède, T. Gabsi, L. Simoulin, N. Striebig, M. Campillo, A. Deschamp, J. Hinderer, J.J. Lévêque, J.P. Montagner, L. Rivéra, W. Benz, D. Breuer,

- P. Defraigne, V. Dehant, A. Fujimura, H. Mizutani, J. Oberst, The NetLander very broad band seismometer. *Plan. Space Sci.* **48**, 1289–1302 (2000). doi:[10.1016/S0032-0633\(00\)00110-0](https://doi.org/10.1016/S0032-0633(00)00110-0)
- P. Lognonné, B. Mosser, Planetary seismology. *Surv. Geophys.* **14**(3), 239–302 (1993)
- R.D. Lorenz, S. Kedar, N. Murdoch, P. Lognonné, T. Kawamura, D. Mimoun, W.B. Banerdt, Seismometer detection of dust devil vortices by ground tilt. *Bull. Seismol. Soc. Am.* (2015). doi:[10.1785/0120150133](https://doi.org/10.1785/0120150133)
- T.Z. Martin, Mass of dust in the martian atmosphere. *J. Geophys. Res., Planets* **100**(E4), 7509–7512 (1995)
- O. Melnik, M. Parrot, Electrostatic discharge in martian dust storms. *J. Geophys. Res. Space Phys.* **103**(A12), 29107–29117 (1998)
- D. Mimoun, J. Gagnepain-Beyneix, P. Lognonné, T. Nébut, D. Giardini, W.T. Pike, U. Christensen, A. van den Berg, P. Schibler, SEIS Team, The SEIS experiment: instrument signal to noise study, in *Seventh International Conference on Mars*. LPI Contributions, vol. 1353, 2007, p. 3279
- D. Mimoun, P. Lognonné, W. Banerdt, K. Hurst, S. Deraucourt, J. Gagnepain-Beyneix, T. Pike, S. Calcutt, M. Bierwirth, R. Roll et al., The InSight SEIS experiment, in *Lunar and Planetary Science Conference*, vol. 43, 2012
- N. Murdoch, B. Kenda, T. Kawamura, A. Spiga, P. Lognonné, D. Mimoun, W.B. Banerdt, Estimations of the seismic pressure noise on Mars determined from large eddy simulations and demonstration of pressure decorrelation techniques for the insight mission. *Space Sci. Rev.*, 1–27 (2016a)
- N. Murdoch, D. Mimoun, R.F. Garcia, W. Rapin, T. Kawamura, P. Lognonné, D. Banfield, W.B. Banerdt, Evaluating the wind-induced mechanical noise on the insight seismometers. *Space Sci. Rev.*, 1–27 (2016b). doi:[10.1007/s11214-016-0311-y](https://doi.org/10.1007/s11214-016-0311-y)
- Y. Nakamura, D.L. Anderson, Martian wind activity detected by a seismometer at viking lander 2 site. *Geophys. Res. Lett.* **6**(6), 499–502 (1979)
- M.P. Panning, É. Beucler, M. Drilleau, A. Mocquet, P. Lognonné, W.B. Banerdt, Verifying single-station seismic approaches using Earth-based data: preparation for data return from the InSight mission to Mars. *Icarus* **248**, 230–242 (2015). doi:[10.1016/j.icarus.2014.10.035](https://doi.org/10.1016/j.icarus.2014.10.035)
- M.P. Panning, P. Lognonné, W.B. Banerdt, R. Garcia, M. Golombek, S. Kedar, B. Knapmeyer-Endrun, A. Mocquet, N.A. Teanby, J. Tromp et al., Planned products of the Mars structure service for the insight mission to Mars. *Space Sci. Rev.*, 1–40 (2016)
- J. Peterson, Sts 2 manual. USGS Open file report n°93-322 (1993a)
- J. Peterson, Trillium compact manual. USGS Open file report n°93-322 (1993b)
- J. Peterson et al., Observations and modeling of seismic background noise (1993)
- L. Pou, D. Mimoun, R. Garcia, P. Lognonné, W.B. Banerdt, Ö. Karatekin, V. Dehant, P. Zhu, Mars deep internal structure determination using Phobos tide measurement strategy with the SEIS/InSight experiment, in *EGU General Assembly Conference Abstracts*, vol. 18, 2016, p. 8724
- A.T. Ringler, R. Sleeman, C.R. Hutt, L.S. Gee, Seismometer self-noise and measuring methods, in *Encyclopedia of Earthquake Engineering*, ed. by M. Beer, I.A. Kougoumtzoglou, E. Patelli, I.S.-K. Au (Springer, Berlin, 2014), pp. 1–13. doi:[10.1007/978-3-642-36197-5_175-1](https://doi.org/10.1007/978-3-642-36197-5_175-1)
- A. Ringler, C. Hutt, Self-noise models of seismic instruments. *Seismol. Res. Lett.* **81**(6), 972–983 (2010)
- G. Sorrells, J.A. McDonald, E.T. Herrin, Ground motions associated with acoustic waves. *Nature* **229**(1), 14–16 (1971)
- G.G. Sorrells, A preliminary investigation into the relationship between long-period seismic noise and local fluctuations in the atmospheric pressure field. *Geophys. J. Int.* **26**(1–4), 71–82 (1971)
- A. Spiga, F. Forget, A new model to simulate the martian mesoscale and microscale atmospheric circulation: validation and first results. *J. Geophys. Res., Planets* **114**(E2) (2009)
- J. Stout, T. Zobeck, Intermittent saltation. *Sedimentology* **44**(5), 959–970 (1997)
- G.H. Sutton, G.V. Latham, Analysis of a feedback-controlled seismometer. *J. Geophys. Res.* **69**(18), 3865–3882 (1964). doi:[10.1029/JZ069i018p03865](https://doi.org/10.1029/JZ069i018p03865)
- N.A. Teanby, J. Stevanović, J. Wookey, N. Murdoch, J. Hurley, R. Myhill, N.E. Bowles, S.B. Calcutt, W.T. Pike, Seismic coupling of short-period wind noise through Mars’ regolith for NASA’s InSight lander. *Space Sci. Rev.* (2016). doi:[10.1007/s11214-016-0310-z](https://doi.org/10.1007/s11214-016-0310-z)
- T. Van Hoolst, V. Dehant, F. Roosbeek, P. Lognonné, Tidally induced surface displacements, external potential variations, and gravity variations on Mars. *Icarus* **161**(2), 281–296 (2003)
- R.J. Warburton, J.M. Goodkind, The influence of barometric-pressure variations on gravity. *Geophys. J. Int.* **48**(3), 281–292 (1977). doi:[10.1111/j.1365-246X.1977.tb03672.x](https://doi.org/10.1111/j.1365-246X.1977.tb03672.x)
- F. Widmer, On noise reduction in vertical seismic records below 2 MHz using local barometric pressure. *W. Zörn. Geophys. Res. Lett.* **22**(24), 3537–3540 (1995). doi:[10.1029/95GL03369](https://doi.org/10.1029/95GL03369)